Controlling crystallization dynamics of photovoltaic perovskite layers on larger-area coatings

Linxiang Zeng[a‡], Shi Chen[b‡], Karen Forberich[c], Christoph J. Brabec[d,e] and Yaohua Mai[a], Fei Guo[a,f]

[a]Institute of New Energy Technology, College of Information Science and Technology, Jinan University, Guangzhou 510632, China

[b]Department of Materials Science and Engineering and Academy for Advanced Interdisciplinary Studies, Southern University of Science and Technology, Shenzhen, Guangdong Province 518055, China

[c]Helmholtz Institute Erlangen-Nürnberg for Renewable Energy (IEK-11), Forschungszentrum Jülich GmbH, Immerwahrstraße 2, 91058 Erlangen, Germany

[d]Institute of Materials for Electronics and Energy Technology (i-MEET), Friedrich-Alexander University Erlangen-Nürnberg, Martensstrasse 7, 91058 Erlangen, Germany

[e]Helmholtz-Institute Erlangen-Nürenberg (HIERN), Immerwahrstr. 2, Erlangen, 91058, Germany

[f]Key Laboratory of Advanced Material Processing & Mold (Ministry of Education), Zhengzhou University, Zhengzhou, 450002, China

[‡] These authors contributed equally to this work. *E-mail: yaohuamai@jnu.edu.cn; fei.guo@jnu.edu.cn*

As perovskite solar cells are highly efficient and already meet the efficiency requirement for renewable power generation, more attention is given to the technological barriers such as scalability and stability. In particular, the large efficiency losses associated with upscaling the lab-scale devices to large-area modules represents one of the major hurdles for commercialization. Given the essential role of the perovskite films in device performance, it is of critical importance to develop reliable crystallization protocols to deposit high-quality perovskite layers via scalable methods. This review summarizes recent advances in emerging crystallization protocols for the large-scale deposition of perovskite thin films. The unique merits of the well-developed crystallization strategies, including antisolvent, gas quenching, vacuum quenching, etc. are carefully analyzed and discussed. We highlight that, independent of the coating method, creating intermediate phases to decouple the otherwise overlapped solution coating and crystal growth is essential to realize homogeneous coatings of perovskite thin films. Strategies for enhancing the crystal morphology of perovskite films are presented as well, which is vitally important to realize reproducible manufacturing of large-area modules. This tutorial review assists the screening and development of robust crystallization strategies for scalable deposition of high-quality perovskite films for photovoltaic applications.

1. Introduction

Solution-processable perovskite solar cells (PSCs) combine the unique features of tunable bandgaps,[1] high absorption coefficient,[2] and long carrier diffusion lengths,[3] which are crucial merits for their rapid rise to the forefront of thin-film photovoltaic (PV) technologies. Since the devise of the first solar cell in 2009, the power conversion efficiency (PCE) of PSCs has rocketed from 3.8% to an impressive level of over 25% within just a decade,[4, 5,6] and has already surpassed the record efficiencies of commercially available PV technologies such as mainstream multi-crystalline silicon and conventional inorganic thin-film solar cells.[7, 8] The fast increase in cell performance stems mainly from a combined effort in controlling the perovskite composition,[9] advanced processing,[6] interface engineering,[10-12] and defects passivation.[13-15] Encouragingly, the operational stability of PSCs is also noticeably increasing as one-year stable solar devices tested under one-sun illumination and at elevated operating temperatures have been reported.[16] This rapid progress in fabrication of high efficiency and long-term stable devices envisages a bright prospect for the commercialization of perovskite PV technology.

Another intriguing advantage of PSCs is that the perovskite absorber layers consist of inexpensive raw materials that can be easily synthesized and are soluble in common organic solvents, including N,N-dimethylformamide (DMF), dimethyl sulfoxide (DMSO), and γ-butyrolactone (GBL). Accordingly, thin films of perovskites can be readily deposited from solution by various coating techniques such as spin-coating,[6] doctor blading,[17] slot-die coating,[18] spray coating,[19] and inkjet printing[20] etc. Most of these fabrication techniques are compatible with industrial roll-to-roll manufacturing processes, allowing to upscale the perovskite PV technology via printing methods.[21] Furthermore, a relatively low annealing temperature typically between 100–150 °C is sufficient for nucleation and crystal growth, rendering the perovskites deposition compatible with flexible polymer substrates.

It is widely acknowledged that the crystal morphology of perovskite layers plays an essential role in determining solar cell performance.[6, 22] Obtaining a uniform, dense and pinhole-free perovskite layer with minimal structural defects is a prerequisite to deliver high device performance. At present, the spin-coating method is predominately used in laboratories to deposit small-area PSCs, leading to continually updated efficiency records.[6, 23] Unfortunately, the biggest bottleneck of spin-coating is that it is limited in size nor can be transferred to other scalable coating lines. Indeed, the size of perovskite films prepared by spin-coating is generally limited to 5×5 cm^2 and probably can be expanded to silicon wafer size level. It is therefore imperative that scalable coating methods can be used to deposit high-quality perovskite films in large-areas and in a high-throughput manner. However, the paramount challenge to realize high-quality perovskite films via printing methods is that the two critical steps, nucleation and crystal growth, usually take place within seconds and overlap each other, making perovskite crystallization intractable.[24] In this context, controlling the crystallization kinetics during perovskite formation is highly demanding for large-scale manufacturing of perovskite thin films.

In this review, we provide an overview on the emerging crystallization technologies that have been proposed for the scalable preparation of perovskite thin films. In contrast to the previous review papers which mainly focus on the implementation of different coating methods,[25-28] we summarize the recent achievements in scalable coating perovskites by classifying the key crystallization technologies. Several crystallization protocols including hot-casting, solvent extraction, vacuum extraction, gas quenching, etc. are carefully discussed to distinguish their viability for scalable coating of high-quality perovskite films by a specific processing method. Particular attention is paid to the scientific challenges of growing dense and uniform perovskite thin films. Additionally, strategies based on post-treatment for improving the morphology of already formed perovskites are presented. Finally,

we provide an outlook on the efficiency deficit associated with upscaling, as well as the key considerations of the stability and toxicity of the PSCs.

2. Nucleation and crystal growth of polycrystalline perovskite

The photovoltaic performance of PSCs depends largely on the crystal morphology of the perovskite absorber layer. In particular, up-scaling PSCs requires coating perovskite thin films uniformly over large-areas without pinholes. However, it is often encountered that without delicately controlling the crystallization process, the obtained perovskite films exhibit incomplete surface coverage due to the tendency of preferential growth toward a dendritic structure,[29, 30] which is detrimental for device performance due to leakage paths. Given the crucial importance of crystallization dynamics in determining the morphology of the final perovskite layer, we start with a comprehensive analysis on the nucleation and crystal growth mechanism of perovskite thin films formation.

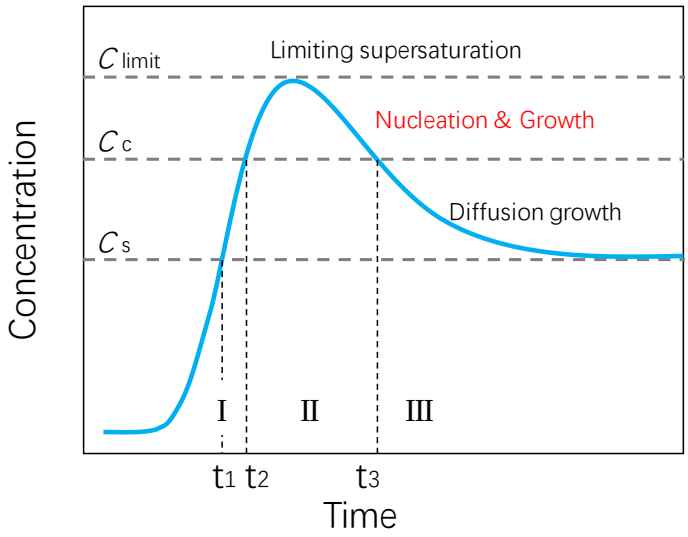

Figure 1. The LaMer model of nucleation and crystal growth.

The preparation of perovskite polycrystalline films from precursor solution involves two important processes, the nucleation followed by the growth of the crystals. It is well accepted that the final crystal morphology of the perovskite film depends strongly on the rates of the two processes, which are closely related to the constantly changing concentrations of the

precursor wet film. The concentration change of a precursor solution as a function of time can be illustrated qualitatively by the LaMer diagram (**Figure 1**). It can be observed that, with the evaporation of the solvent, the solution concentration increases and reaches the saturation concentration (denoted as C_s on the graph) at a time of t_1. However, the formation of nuclei at this stage (stage I) is prohibited until the critical concentration (denoted as C_c) is reached at a time t_2, owing to the fact that the energy barrier for nucleation has to be overcome. When the concentration is higher than C_c (stage II), both nucleation and crystal growth take place. The solution concentration increases constantly as the solvent continuously evaporates, which results in a fast rate of nucleation. Due to the competition between the solvent evaporation and the solute consumption by crystal growth, the concentration of the solution then starts to decrease and finally drops below C_c. It is seen from stage I and II that the nucleation rate increases with increased supersaturation, a higher and faster supersaturation will lead to higher nucleation rate and density (more nuclei) and, thus, a larger number of smaller crystals. In the third stage, no more nuclei are created but grains will continuously grow until the concentration drops below C_s.

3. Lessons learned from antisolvent extraction in spin coating

Since the two important processes, nucleation and crystal growth, are strongly related to the concentration of the solution or, in other words, to solvent evaporation, it is important to understand whether a fast or slow solvent evaporation rate is more favorable for producing high-quality photovoltaic perovskite layers. The classic crystallization protocol based on the antisolvent extraction which is commonly used for spin coating provides a sound hint illustrating the importance of the creation of a supersaturation state in a very short time.[6] After adding the orthogonal solvent just few seconds before the end of the substrate rotation, rapid nucleation takes place which brings solution concentration above the C_c. Therefore, the nuclei are created on the substrate until the substrate is fully covered and in parallel the

crystal growth time is reduced significantly during the spin coating process. The subsequent crystal growth is realized by applying a thermal annealing, yielding a uniform perovskite film with small grain size and full surface coverage.

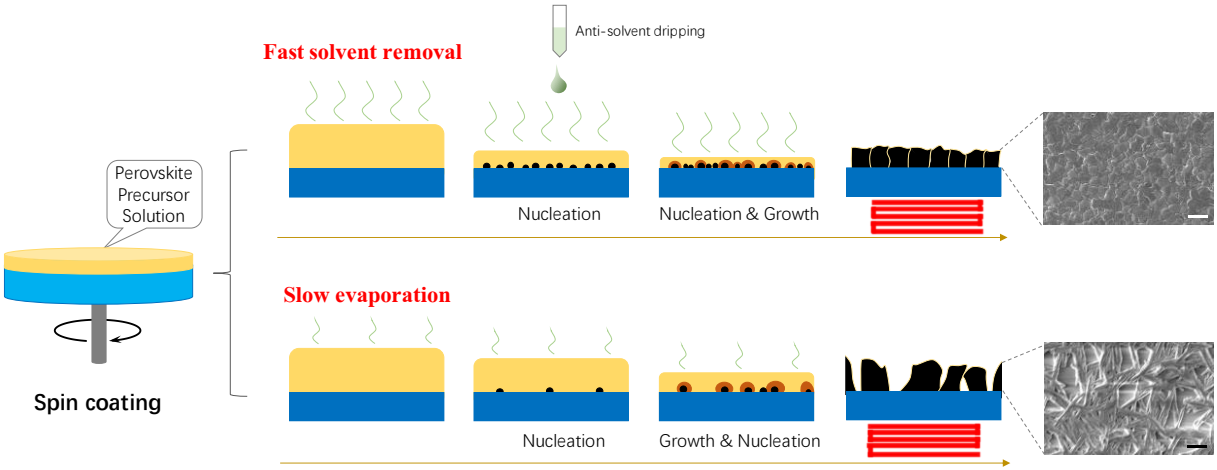

Figure 2. Schematic illustration of the perovskite film growth with a fast (top) and slow (bottom) solvent removal of the precursor wet film. The scale bars in SEM images are 1 μm.

Based on the above analysis of the LaMer model and the classic antisolvent approach, it can be concluded that if a fast evaporation of the solvent takes place, a rapid supersaturation can be reached with solution concentration continuously maintained above C_c. As a result, the nucleation rate will quickly increase and, meanwhile, the crystal growth time will decrease, leading to more nuclei as well as smaller and more uniform grains (**Figure 2**). Therefore, to fabricate a uniform perovskite layer with complete surface coverage, the crystal growth rate should be slowed down and, more importantly, the number of nuclei should be increased during a short period at the early stage of precursor film drying. On the other hand, if the solvent evaporation is slow, the solution concentration drops below C_c but remains larger than C_s, which leads to fast and constant crystal growth. As a consequence, no more nuclei are generated but grain growth continues. This eventually brings about relatively small numbers of large grains with macroscopic inhomogeneity and incomplete surface coverage (**Figure 2**).

4. One-step versus sequential two-step

From the deposition procedure point of view, perovskite thin films can be processed from solution by either one-step or two-step sequential deposition. Both approaches require delicate control over the crystallization kinetics to achieve dense and uniform perovskite films with minimal structural defects. In the one-step deposition method, a perovskite film is produced from a precursor solution mixture of organic halide and lead halide. The precursor solution can be deposited by spin coating or other printing methods, followed by the conversion to perovskite crystals upon removing the solvents.[6] Although the one-step method is relatively simple and inexpensive compared to the two-step procedure, it is challenging to produce uniform and compact perovskite films without delicately controlling the nucleation and crystal growth during film formation.

In comparison, perovskite films are produced through a conversion reaction of lead halide and organic halide in the two-step sequential deposition.[31-33] As a first step, lead iodide (PbI_2) is deposited by spin coating or another coating methods, and then dipped into a methylammonium iodide (MAI) solution and converted to a perovskite.[31, 32] Alternatively, sequentially coating the two precursor ingredients offers a more promising approach in terms of continuous high-throughput manufacture.[34, 35] During the conversion reaction, MAI molecules are inserted into the PbI_2 structure, and the yellowish color of the PbI_2 film is changed to dark brown, indicating the formation of perovskite crystals. It has been reported that the difference in the bulk lattice energy and the strong ionic interaction between the two materials are the driving force for inducing this reaction.[31] PbI_2 crystals feature strong intralayer chemical bonding but weak interlayer van der Waals interactions; therefore, MAI molecules can be easily inserted between these layers. In a two-step deposition process, the morphology of perovskite films tends to be strongly dependent on PbI_2 film microstructure.[35]

Controlling the uniformity of the PbI_2 film and its reactivity with MAI is the key factor for determining the quality of the perovskite layer.

5. Crystallization protocols for large-area coating of perovskite films

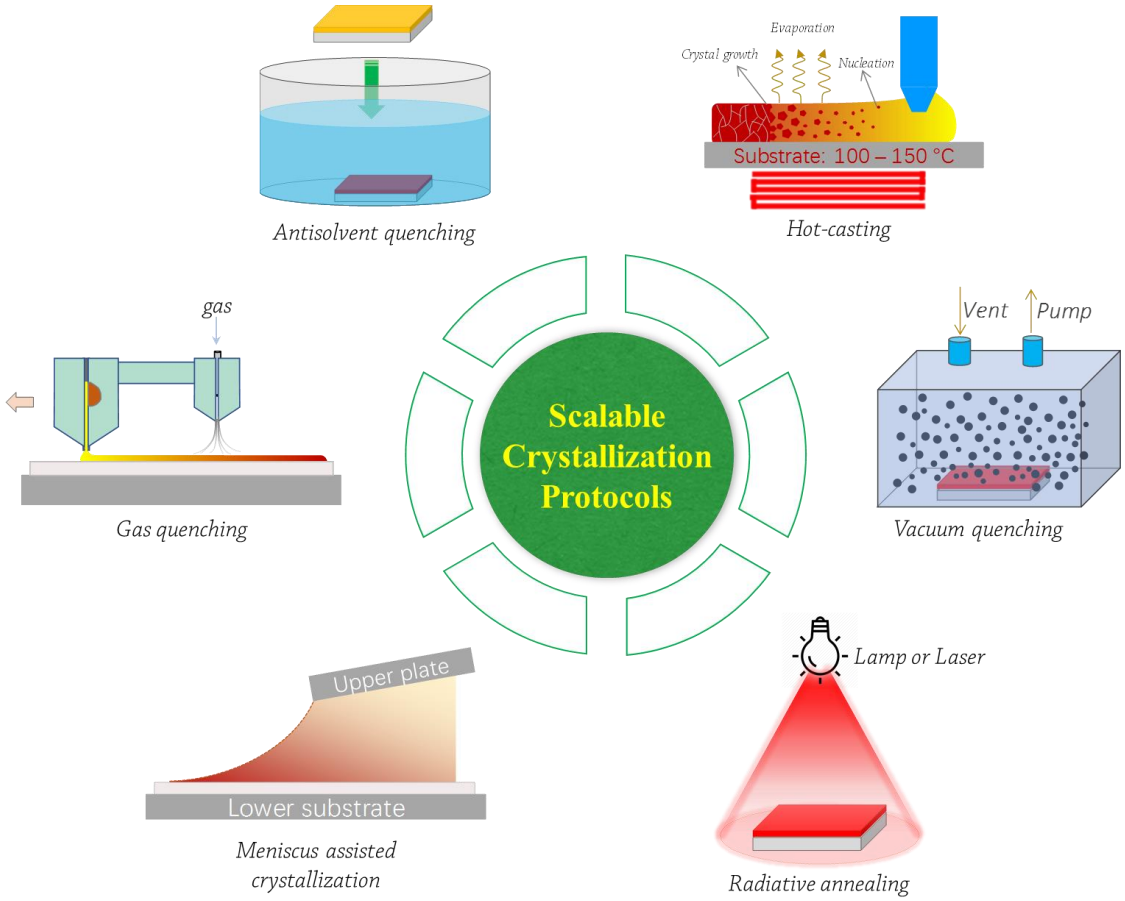

Figure 3. Crystallization protocols that have been developed for the deposition of perovskite thin films by scalable coating methods.

The preparation of a uniform and pinhole-free perovskite film over large-areas plays a key role in delivering high performance perovskite solar cells and modules. It has been stated that the occurrence of the three stages (solution state, nucleation, and crystal growth) described in the LaMer graph strongly depends on the drying kinetics of the freshly coated perovskite precursor solution, which is, in principle, independent of coating method. Therefore, the choice of quenching methods for the generation of the supersaturation state is of great importance to tune the balance between the nucleation and crystal growth. A rapid solvent removal from the perovskite precursor solution results in fast supersaturation,

leading to more nucleation with shorter grain growth time, which is beneficial for preventing the aggregation and migration of the solute. Coupled with more nuclei, a shorter growth time suppresses the overgrowth of individual nuclei into large dendritic structures. In this section, we review the emerging crystallization approaches including hot-casting, solvent extraction, gas quenching, vacuum quenching and irradiation etc., that are capable of rapidly removing the solvent of printed precursors and, thereby facilitating the growth of homogenous and dense perovskite thin films (**Figure 3**). The photovoltaic parameters of the scalable deposited perovskite solar devices introduced in this section are summarized in **Table 1**.

Table 1. Photovoltaic parameters of scalable deposited perovskite solar cells and submodules fabricated by different crystallization protocols.

Crystallization protocol	Coating method	Coating temperature	Perovskite composition	Active area [cm^2]	V_{OC} [V]	J_{SC} [mA cm^{-2}]	FF [%]	PCE [%]	Note	Reference
Hot-casting	Blade-coating	125 °C	$MAPbI_3$	0.725	1.05	21.8	66	15.1	One-step	17
Hot-casting	Blade-coating	100-145 °C	$MA_{0.6}FA_{0.38}Cs_{0.02}PbI_{2.975}Br_{0.025}$	-	1.09	23.1	77	19.5	One-step	37
Hot-casting	Blade-coating	100 °C	$MAPbI_3$	-	1.04	21.7	75	16.9	One-step	38
		145 °C	$FA_{0.4}MA_{0.6}PbI_3$	-	1.03	23.0	77	18.3	One-step	
Hot-casting	Blade-coating	135 °C	$MAPbI_3$	0.1	0.92	23.58	73	15.8	One-step	40
Hot-casting	Blade-coating	150 °C	$MAPbI_3$	0.08	1.1	22.7	81	18.85	One-step	41
Hot-casting	Blade-coating	150 °C	$MAPbI_3$	0.08	1.18	22.5	81.7	21.7	One-step	42
				1.1	1.14	22	80	20		
			$Cs_{0.05}FA_{0.70}MA_{0.25}PbI_3$	0.08	1.06	23.4	68.4	17		
			$Cs_{0.2}FA_{0.8}Pb(I_{0.6}Br_{0.4})_3$	0.08	1.26	15.6	77.5	15.2		
Hot-casting	Slot-die	130 °C	$MA_{0.6}FA_{0.38}Cs_{0.02}PbI_{2.975}Br_{0.025}$	0.1	1.00	21.35	68.65	14.66	One-step	43
Hot-casting	Blade-coating	-	$Cs_{0.05}FA_{0.70}MA_{0.25}PbI_3$	0.08	1.18	23.6	79	22	One-step	47
Hot-casting	Blade-coating	145 °C	$MAPbI_3$	0.075	1.12	22.4	81	20.3	One-step	50
				33.0	1.07	19.5	72.1	15.3		
				57.2	1.07	20.2	66.1	14.6		
Hot-casting	Blade-coating	150 °C	$MAPbI_3$	0.09	1.07	22.67	77.01	18.74	One-step	51
				1.0	1.08	23.17	68.49	17.06		
Hot-casting	Blade-coating	150 °C	$MAPbI_3$	0.09	1.08	22.33	74.21	17.54	One-step	52

Meniscus-assisted solution printing	Blade-coating	60 °C	$FA_{0.85}MA_{0.15}PbI_{2.55}Br_{0.45}$	0.1	1.1	23.2	78.58	20.05	One-step	55
				1	1.09	22.35	73.93	18.02		
Meniscus-assisted soft-covering	Soft-covering	210 °C	$MAPbI_3$	1	1.02	21.8	78.7	17.6	One-step	56
Meniscus-assisted soft-covering	Soft-covering	Room-temperature	$MAPbI_3$	1	1.12	22.6	76.2	19.3	One-step (Pressure-assisted solvent-free)	58
Meniscus-assisted soft-covering	Soft-covering	80 °C	$MAPbI_3$	0.09	1.07	21.5	77	17.7	Two-step	59
				0.09	1.09	19.5	72.3	15.3	Two-step (flexible)	
				5	1.03	21.5	70.1	15.5	Two-step	
Antisolvent quenching	Blade-coating	Room temperature	$MA_{0.7}FA_{0.3}PbI_3$	10.36	4.38	4.80	72	15.6	Mini-module	67
Antisolvent quenching	Blade-coating	Room temperature	$MAPbI_3$	0.12	1.08	22.2	77.1	18.55	One-step	68
				1.2	1.11	21.38	72.9	17.33		
				12.6	4.396	-	-	14.06	Mini-module	
Antisolvent quenching	Slot-die	Room temperature	$MAPbI_3$	0.06	1.10	21.5	76	18	One-step	69
Gas quenching	Slot-die	65 °C	$MAPbI_3$	0.0625	0.73	16.8	75.6	9.2	One-step	18
Gas quenching	Blade-coating	Room temperature	$MAPbI_3$	0.1				13.3	Two-step	72
				10.1				10.4		
				100				4.3		
Gas quenching	sequential slot-die coating	PbI_2: Room temperature MAI: 70 °C	$MAPbI_3$	0.1	0.95	19.89	53.67	10.14	Two-step	73
Gas quenching	Drop-casting	Room temperature	$MAPbI_3$	0.09	1.09	23.46	78.51	20.08	One-step	74
				1	1.05	22.94	74.52	18.02		
Gas quenching	Bar-coating	-	$GA_{0.12}MA_{0.88}PbI_3$	0.125	1.19	21.03	78	19.44	One-step	79

				16				13.85		
Gas quenching	Blade-coating	Room temperature	$MAPbI_3$	0.08 63.7	1.13 18.9	23 75.5	81.8 76.2	21.3 16.9	One-step	76
Gas quenching	Blade-coating	Room temperature	$MAPbI_3$	0.08 42.9	1.092 13.142	22.83 19.71	79.1 73.5	19.72 15.86	One-step	77
Vacuum quenching	Inkjet printing	23 °C	$Cs_{0.10}FA_{0.75}MA_{0.15}Pb(Br_{0.15}I_{0.85})_3$	0.105	1.11 (1.06)	24.6 (24.3)	80 (70)	21.6 (18.1)	One-step	20
Vacuum quenching	Blade-coating	Room temperature	$MAPbI_3$	0.09	1.04	21.36	75	16.71	Two-step	88
Vacuum quenching	Blade-coating	Room temperature	$MAPbI_3$	0.09 1 10.08	1 1.01 3.87	22.58 21.70 4.93	80 67.15 59	18.06 14.72 11.25	One-step	89
			$FA_{0.95}Cs_{0.05}PbI_3$	0.09	1.01	22.81	72.20	16.63		
			$FA_{0.6}MA_{0.4}Pb(I_{0.6}Br_{0.4})_3$	0.09	1.07	16.59	69.50	12.34		
Vacuum quenching	Blade coating	-	$MAPbI_3$	0.1 1.96	1.12 1.09	23.27 22.64	77.63 73.66	20.46 18.26	One-step	90
Vacuum quenching	Blade coating	-	$MAPbI_3$	0.12 16	1.07 3.98	23.11 5.82	76 68	18.25 15.79	One-step	91
Vacuum quenching	Blade coating	Room temperature	$MAPbI_3$	0.09 1	1.09 1.10	21.98 20.97	81 72	19.41 16.61	One-step (Flexible)	92
Vacuum quenching	Blade-coating	Room temperature	$(FASnI_3)_X(MAPbI_3)_Y$	0.09 1	0.78 0.78	24.90 23.46	78 68	15.15 12.44	One-step	93
Vacuum quenching	Blade-coating	Room temperature	$(MAPbI_3)_{0.75}(FASnI_3)_{0.25}$	0.09 1	0.79 0.80	28.42 26.58	78 65	17.51 13.88	One-step	94

Vacuum quenching	Spray coating	40 °C	$CsI_{0.05}((FAPbI_3)_{0.85}(MAPbBr_3)_{0.15})_{0.95}$	0.026	1.10	22.3	73	17.8	One-step	97
Vacuum quenching	Inkjet printing	Room temperature	$Cs_{0.1}FA_{0.75}MA_{0.15}(I_{0.75}Br_{0.15})_3$	0.105	1.02	23.6	71.5	17.2	One-step	98
Vacuum quenching	Blade-coating	Room temperature	$MAPbI_3$	0.09	1.19	22.36	75.7	20.14	One-step	118
				10.08	4.67	4.96	66.4	15.38		

Note: V_{OC}: Open-circuit voltage; J_{SC}: Short-circuit current density; FF: Fill factor.

5.1 Hot-casting

Hot-casting is a straightforward method of expediting solvent removal from a printed wet film and induces rapid supersaturation. Hot-casting can be facilely carried out by coating a perovskite solution on a preheated substrate. In 2015, Mohite and coauthors reported the fabrication of perovskite thin films based on hot-casting crystallization by spin coating.[36] It is found that the grain size of perovskite increases with the increase of substrate temperature. Crystal grains in millimeter scale are obtained when processed at temperatures up to 190 °C. They also discovered that the presence of a small amount of high boiling-point solvent is beneficial for obtaining large grains due to prolonged crystal growth. Benefiting from the suppressed charge recombination and improved carrier mobility, the photovoltaic performance of perovskite devices is greatly enhanced as a result of large grain size.

Since controlling the substrate temperature in scalable coating methods is more convenient than in spin-coating, the hot-casting strategy has been applied to deposit thin films of perovskites by various printing methods, such as blade coating,[17, 37-43] spray coating,[44, 45] dip coating.[46] Early in 2015, Deng et al. for the first time, reported blade-coating of methylammonium lead triiodide ($MAPbI_3$) perovskite films on a preheated substrate (**Figure 4a**).[17] They found that the substrate temperature plays an important role in determining crystal morphology of the perovskite films. A long time is required for drying the precursor wet film when blading at substrate temperature of 100 °C or lower, resulting in non-uniform perovskite film with needle-like crystal domains and incomplete surface coverage (**Figure 4b**). Blading perovskite solution at 125 °C ensures rapid supersaturation of the precursor sheet, which is found to be the optimum temperature for obtaining continuous and smooth films (**Figure 4c**). Perovskite solar cell prepared by hot-casting yields an efficiency of 15.1%. Further increasing the substrate temperature to 145 °C, close to the boiling point of the

solvent DMF, is also able to produce smooth film with complete coverage. However, such a high temperature is found to decompose the prepared $MAPbI_3$ films as well.

Hot-casting is also demonstrated to be effective for compositional engineering of formamidinium (FA)-based perovskites by blade coating. Compared to their MA-based counterparts, FA-based perovskites exhibit higher thermal stability and smaller bandgaps, which are more favorable for solar cell efficiency and operation. By taking advantage of the facile temperature controlling capability of blade coating, Deng *et al.* fabricated α-phase FA-based perovskite films by blade coating a solution mixture of FAI:MAI:PbI_2 on preheated substrates.[38] They found that a high temperature of 145 °C is required to obtain α-phase pure $FAMAPbI_3$. Completely suppressing the formation of δ-phase at temperatures lower than 100 °C was found to be difficult. To further stabilize the α-phase FA-based perovskite, Tang *et al.* added a very small amount of Cs cations into the precursor solution to enhance the phase purity of FA-based perovskite films.[37] It is found that the incorporation of 2 mol% Cs reduces the Urbach energy and enhances charge carrier lifetime in the films. In a very recent study, Wu *et al.* incorporated a small amount of phenylethylammonium chloride (PEACl) in FA-based triple-cation perovskite precursor to suppress the formation of δ-phase by hot-casting (**Figure 4d**).[47] The introduced Cl anion is able to modulate the crystal growth to obtain perovskite films with high crystallinity and large grains (**Figure 4e**). The hot-casted solar cells achieve high efficiencies of 22.0% with a V_{OC} of 1.18 V (**Figure 4f**), corresponding to a very small voltage deficit of 0.33 V for the bandgap of 1.51 eV. Moreover, the stable α-phase FA-alloyed perovskite gives rise to a significantly enhanced operational stability of the devices with 96% of the initial efficiency retained under one sun illumination for 500 h.

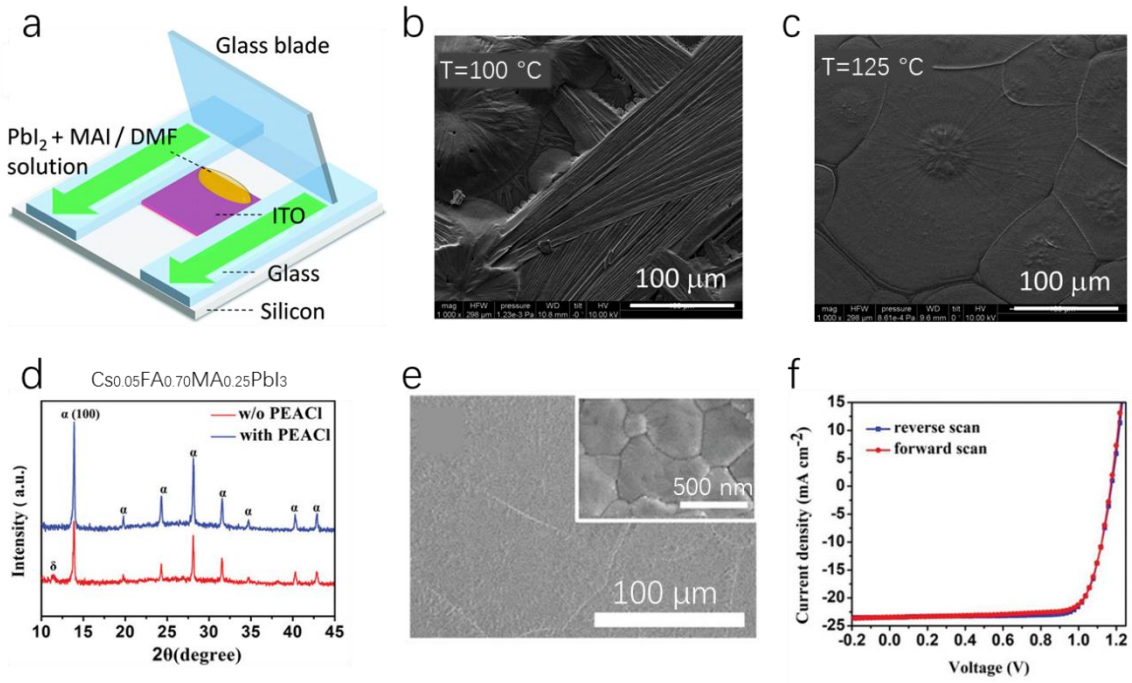

Figure 4. (**a**) Schematic illustration of the blade-coating of perovskite film. Top-view SEM images of the $MAPbI_3$ films deposited at a substrate temperature of 100 °C (**b**) and 125 °C (**c**). Reproduced with permission.[17] Copyright 2015, Royal Society of Chemistry. (**d**) XRD spectra of the pristine and PEACl-incorporated triple cation perovskite films which were prepared by blade coating. (**e**) SEM images of the PEACl incorporated perovskite film. (**f**) J-V curves of the champion solar cells with reverse and forward voltage scan. Reproduced with permission.[47] Copyright 2020, Wiley-VCH.

It should be noted that the surface energy of the substrate largely influences the solution drying kinetics and thereby greatly impacts the crystal morphology of the final perovskite film.[48] In particular, it is challenging to coat a perovskite precursor solution on top of hydrophobic interfaces due to severe de-wetting problems.[49] To overcome this limitation, Deng *et al.* proposed a surfactant-controlled ink drying as a viable solution to alter the fluid drying dynamics during hot-casting of perovskite films by blade coating.[50] Incorporating L-α-Phosphatidylcholine as surfactant into the precursor, they printed the perovskite solution with blading speeds higher than 50 mm s^{-1}, which guarantees that the coated precursor is stays wet before the substrate is moved from the blade coater to a hot plate for thermal annealing. They found that the solution flow toward crystal islands is originated from the

surface tension gradient, which leads to rough and discontinuous crystal morphology. To suppress the solution flow during the solution drying, they incorporated a very small amount of surfactant (20 ppm) to create a "Marangoni flow", which originates from the gradient of surfactant concentration from the island periphery to the solution, As a result, the "Marangoni flow" counteracts and suppresses the original solution flow. They further showed that the surfactants with charged quarteramonium ions not only improve the wettability of the solution on hydrophobic interfaces, but also passivate the defect states in perovskite films. Benefiting from the pinhole-free and smooth film with reduced trap states, solar modules with stabilized PCEs up to 15.3% and 14.6% are demonstrated with active areas of 33.0 and 57.2 cm^2, respectively.

Understanding the underlying physics of the hot casting-based crystallization is highly desired to establish reproducible and scalable processes. To this end, comprehensive investigations on the structural evolution and crystal growth mechanism using time-resolved grazing-incidence wide-angle X-ray scattering (GIWAXS) and time-resolved optical microscopy have been conducted (**Figure 5a** and **5b**).[51-53] It is found that the participation of intermediate phases plays a key role in hot casting crystallization for both spin coating and blade coating. A slow solvent removal during blade coating at room temperature leads to indirect crystallization from the precursor sol-gel to perovskite crystals with the participation of intermediate phases, resulting in inferior perovskite film with a dendritic crystal morphology (**Figure 5c**). In contrast, blade coating at high substrate temperatures ensures fast removal of solvent, resulting in direct crystallization from disordered sol-gel to $MAPbI_3$ crystals by skipping the formation of intermediate phases (**Figure 5d**). As a result, dense perovskite films with high crystallinity and good photophysical properties are obtained by coating the precursor films at a substrate temperature of 150 °C. Planar photovoltaic cells

based on the perovskite films fabricated via direct crystallization deliver efficiencies of 18.74% (0.09 cm^2) and 17.06% (1 cm^2).[51]

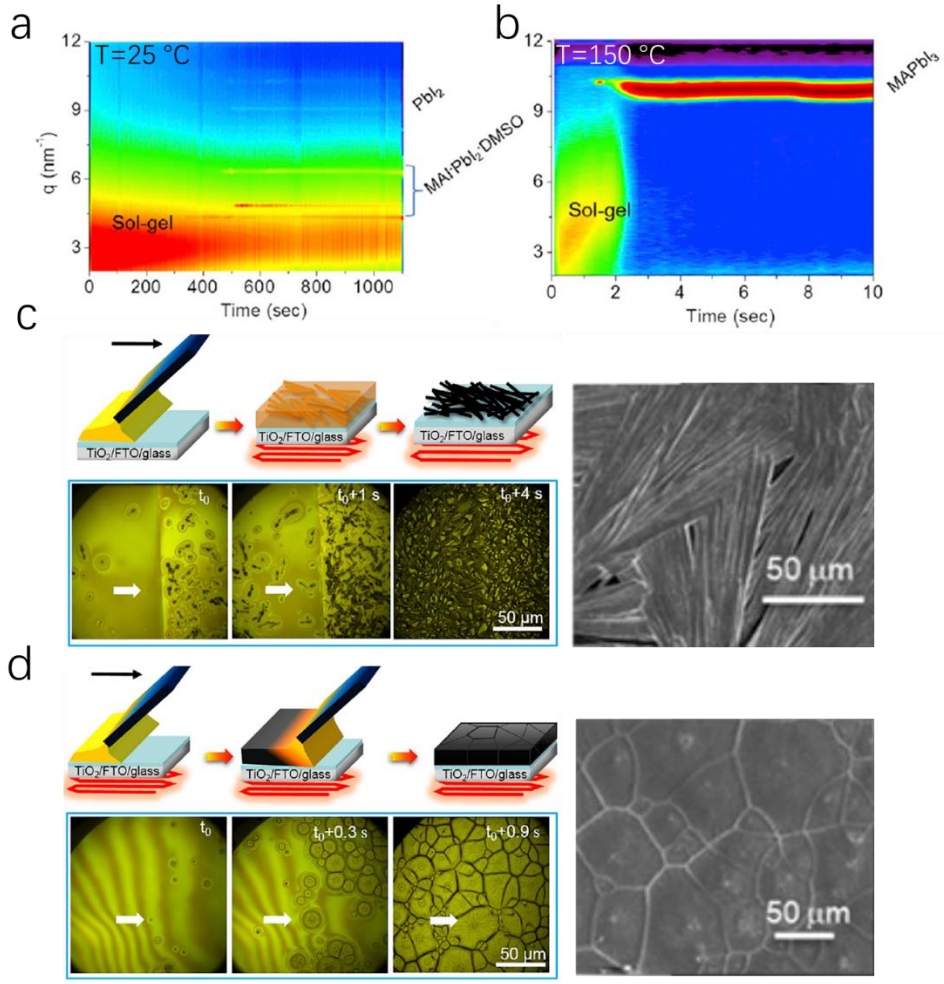

Figure 5. In situ GIWAXS characteristics performed during blade-coating at a substrate temperature of 25 °C (**a**) and 150 °C (**b**) Reproduced with permission.[51] Copyright 2018, Elsevier. Schematic representation of the $MAPbI_3$ film formation mechanism and SEM micrographs representing low (**c**) and high (**d**) blade-coating temperatures. Reproduced with permission.[52] Copyright 2018, American Chemical Society.

Similar to the hot-casting procedure, a hot dip-coating technique was also developed, during which the preheated substrates is dipped into a hot perovskite precursor solution.[54] Perovskite crystallizes on the substrate instantaneously as the substrate is drawn out from the solution. Solar cells based on hot-dipping coating yields a decent PCE of 12.4%. Given that dip-coating is one of the mature large-scale deposition methods, it is expected that

improved device performance can be achieve using slot-die coating and high throughput roll-to-roll production lines by means of better control film thickness and roughness.

5.2 Meniscus-assisted solution printing

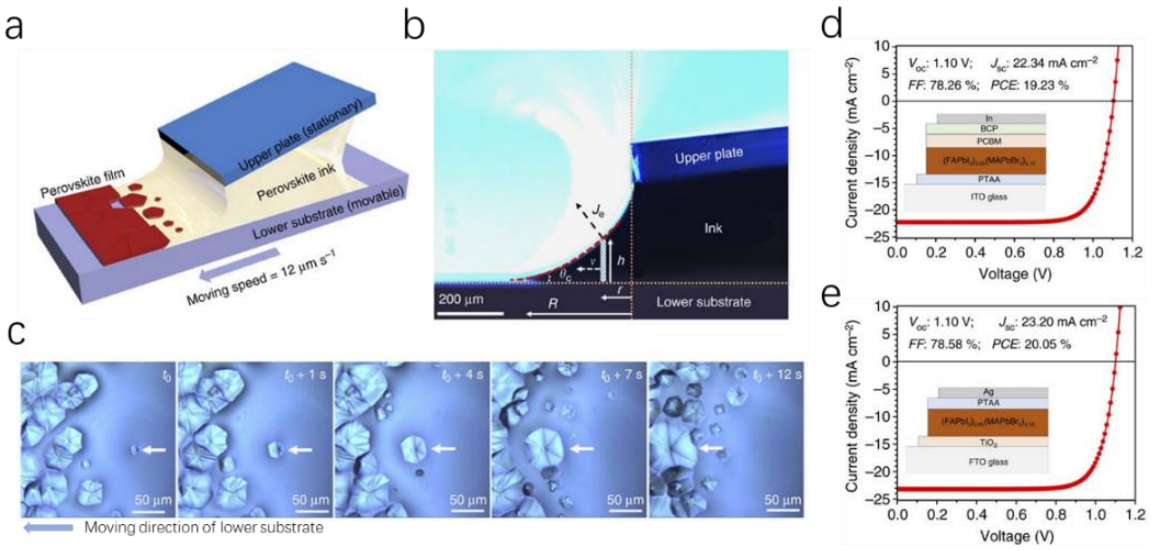

Figure 6. (**a**) Schematic illustration of the meniscus-assisted solution printing of large-grained perovskite films. (**b**) Optical micrograph of the side-view meniscus ink confined between a lower flat, movable substrate and an upper stationary plate. (**c**) Optical micrograph of the microstructural evolution of $FA_{0.85}MA_{0.15}PbI_{2.55}Br_{0.45}$ perovskite grain as a function of time. Current density–voltage (J–V) characteristics of the inverted (**d**) and normal (**e**) structure perovskite solar cell. Reproduced with permission.[55] Copyright 2017, Springer Nature Limited.

Controlling crystallization dynamics during hot casting at high deposition temperatures approaching or exceeding the boiling point of the precursor solvent is found to be challenging. This is because the solute migration and aggregation associated with solution convection is extremely sensitive to coating temperature. Therefore, special care and experienced operation is commonly required for the reproducible production of dense and uniform perovskite layer over large areas. To bypass this limitations, in 2017 He *et al.* developed a meniscus-assisted solution printing (MASP) method to fabricate perovskite films at a much milder temperature (**Figure 6a**).[55] A concave meniscus of the solution at the air/perovskite and ink/substrate is formed due to capillary force (**Figure 6b**). Fast evaporation of solvent is realized at the edge of the meniscus, which promotes the migration

of solute toward the front of the meniscus by outward convection. As a result, a rapid supersaturation is realized at the front of the meniscus, which induces immediate crystallization of the perovskites at mild elevated temperatures. A real-time tracking of the perovskite crystal growth by optical microscopy is shown in **Figure 6c**, which depicts the evolution of a perovskite nucleus into a large-grained microstructure. It is found that the coating speed and the substrate temperature play critical roles in controlling the outward convection during solution drying and the subsequent crystal growth. Using the optimized coating speed of 12 μm s^{-1} along with an optimal substrate temperature of 60 °C, pinhole-free perovskite films with large grain size and preferred orientation are successfully fabricated. Inverted (p-i-n) and normal (n-i-p) structured solar devices with active area of 0.1 cm^2 show stabilized PCEs of 19.1% and 19.9%, respectively (**Figure 6d** and **6e**). A large-area device with an active area of 1 cm^2 is also fabricated, giving a PCE ~17%.

It should be noted that although the MASP is capable of controllable perovskite deposition over large areas, the slow printing speed represents a major limitation, which can prohibit the feasibility for high-throughput roll-to-roll manufacturing. Furthermore, the high sensitivity of the meniscus shape on a variety of factors such as printing speed, gap between the substate and blade, and surface tension of the lower substrate imposes a barrier for the reliable implementation of the technology.

5.3 Meniscus-assisted soft-covering

In 2016, Han and coworkers developed a soft-covering crystallization method for scalable deposition of perovskite films.[56] The soft-covering technology elegantly brings together the unique features of hot-casting and meniscus-assisted crystallization. A soft polymer sheet with high wettability is applied to spread perovskite precursor ink on a preheated substrate (**Figure 7a**). The covering sheet also confines the precursor in the wet state between the substrate and the cover film, thereby preventing the fast evaporation of solvent and the

undesired solute aggregation. Upon peeling off the cover film at a certain speed, a meniscus edge is formed at the interface of substrate, cover film and air. As a result, fast solvent evaporation and crystallization take place instantaneously as the precursor solution is exposed to air. Compared with the spin-coating, perovskite films deposited by soft-covering deposition (SCD) exhibit larger crystal grains (**Figure 7b and 7c**), probably due to retarded crystallization. Inverted solar cells based on the soft-covering deposited perovskite films deliver an efficiency of 17.6% with small hysteresis (**Figure 7b and 7c**). Noticeably, a uniform perovskite thin film of up to 51 cm^2 is prepared using this soft-cover method.

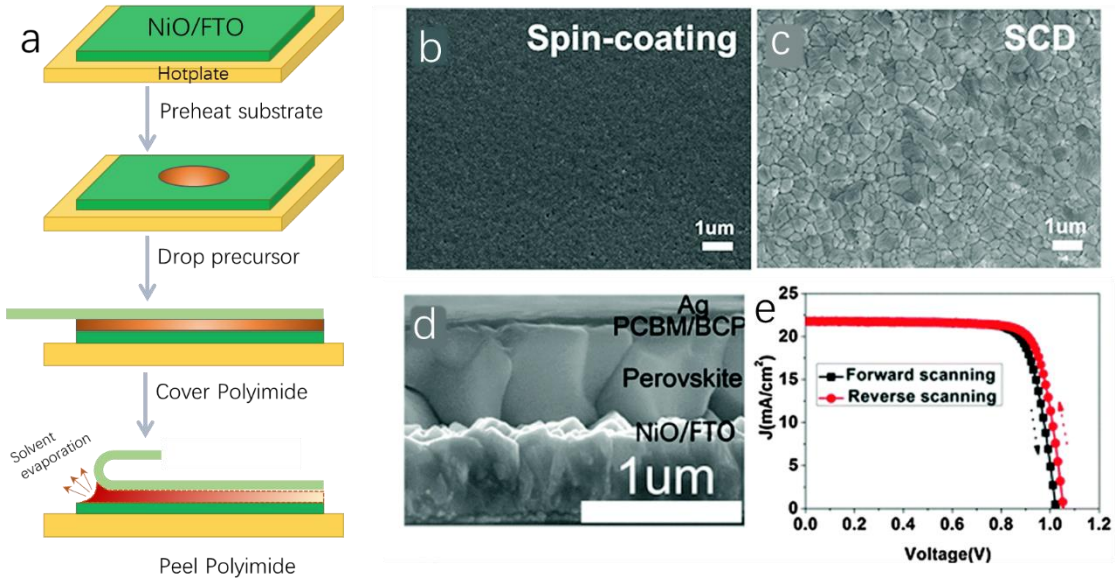

Figure 7. (**a**) Schematic illustration of the soft-cover deposition of perovskite thin films. Perovskite film produced by spin-coating (**b**) and doctor blade coating (**c**). (**d**) Cross sectional SEM image of an inverted perovskite solar device. (**e**). J-V curves of the champion solar cells with reverse and forward voltage scan. Reproduced with permission.[56] Copyright 2016, Royal Society of Chemistry.

It should be noted that the soft-covering process in a single step has to be carried out at a high substrate temperature of 210 °C, which may soften and deform the ultrathin polymer cover sheet, thereby constraining the processing window. Later on, an improved method of low-temperature soft cover-assisted sequential deposition process was developed.[57] By rationally selecting the solvent of inorganic PbI_2, the thermal convection in PbI_2 precursor solution can be well modulated. PbI_2 processed at a low temperature of 80 °C possesses a

smooth morphology without convection-related defects, which is prerequisite for obtaining high-quality perovskite films via sequential two-step deposition. Homogeneous and convection-induced-defects-free $MAPbI_3$ films are obtained by reacting the prepared PbI_2 with MAI solution during capillary immersion. A flexible solar cell based on this method delivers an efficiency of 15.3%.

Crystalline $MAPbI_3$ perovskite as well as their precursors PbI_2 and MAI can react with methylamine gas and result in intermediate phases which are in liquid state under ambient conditions.[58, 59] The formed $MAPbI_3{\cdot}CH_3NH_2$ liquid complex can be further processed by various solution coting methods. Taking this unique feature, Han and coworkers extended the soft cover strategy to prepare high-quality $MAPbI_3$ films by using a high pressure to spread the $MAPbI_3{\cdot}CH_3NH_2$ liquid complex on substrate.[59] A dense and pinhole-free perovskite film with large crystal grains is obtained over a large substrate (8 cm×8 cm). Perovskite solar cells prepared by pressure-assisted soft-covering deliver a PCE of 19.3% (1.0 cm^2). In addition, a 10-subcell series-connected module with an illuminated aperture area of 36.1 cm^2 yields a certified efficiency of 12.1%.

5.4 Antisolvent quenching

It is noticed that in the aforementioned hot-casting and meniscus-assisted methods, the two important processes of perovskite formation, nucleation and crystal growth, take place simultaneously with the perovskite precursor solution deposition, it hence remains a major challenge to tailor the film morphology, crystallinity, and crystal orientation. In this regard, it is of great significance that the nucleation and crystal growth can be decoupled to achieve a more controlled fashion to manipulate the crystal morphology of the perovskite films. First introduced by Seok and coauthors in 2014,[6] antisolvent extraction has been established as an effective and “standard” laboratory technique to prepare high-quality perovskite films of a wide variety of compositions. The antisolvent extraction is based on a fast quenching process,

in which a supersaturation state is formed with a sudden removal of the excess solvent by pouring a large quantity of orthogonal solvent on the spinning perovskite precursor. A large number of antisolvents which are miscible with the perovskite precursor solvent but do not dissolve the perovskite crystals have been investigated, for instance toluene,[6, 60] chlorobenzene,[61] ethyl ether,[62] ethyl acetate,[60] hexane[62] and anisole[63]. It has been proposed that the application of an antisolvent accelerates heterogeneous nucleation with the formation of an intermediate phase. Later studies confirm that the resulting intermediate phase consists of a molecular structure of $MA_2Pb_3I_8 \cdot 2DMSO$,[3, 35-37, 64] which originates from the intercalation of MAI and DMSO into layered PbI_2. Applying thermal annealing to the intermediate phase generates crystalline perovskite films that are smoother and of higher quality than those prepared by spin coating without antisolvent treatment.

At present, antisolvent extraction is implemented primarily in spin-coating process. However, it is generally observed that the time window for dripping antisolvent is very narrow which has to be carried out strictly several seconds after the substrate starts rotation or before the end of rotation. In addition, several key factors such as volume of antisolvent, distance of dripping and the local environment like temperature and solvent atmosphere *etc.* may significantly influence the lab-to-lab or even batch-to-batch variation for PSCs fabrication. Moreover, the antisolvent dripping combined with spin-coating is neither scalable, nor can it be transferred to scalable coating methods and, is thus limited with respect to film area for practical applications. To bypass this limitation, antisolvent bathing has been developed for the fabrication of uniform and dense $MAPbI_3$,[65] which features few appealing attributes including room temperature deposition, rapid crystallization, and film smoothness. The versatility of the antisolvent extraction was demonstrated by the preparation of mixed Sn-Pb perovskite with different bandgaps and semitransparent PSCs for tandem applications.[63, 66]

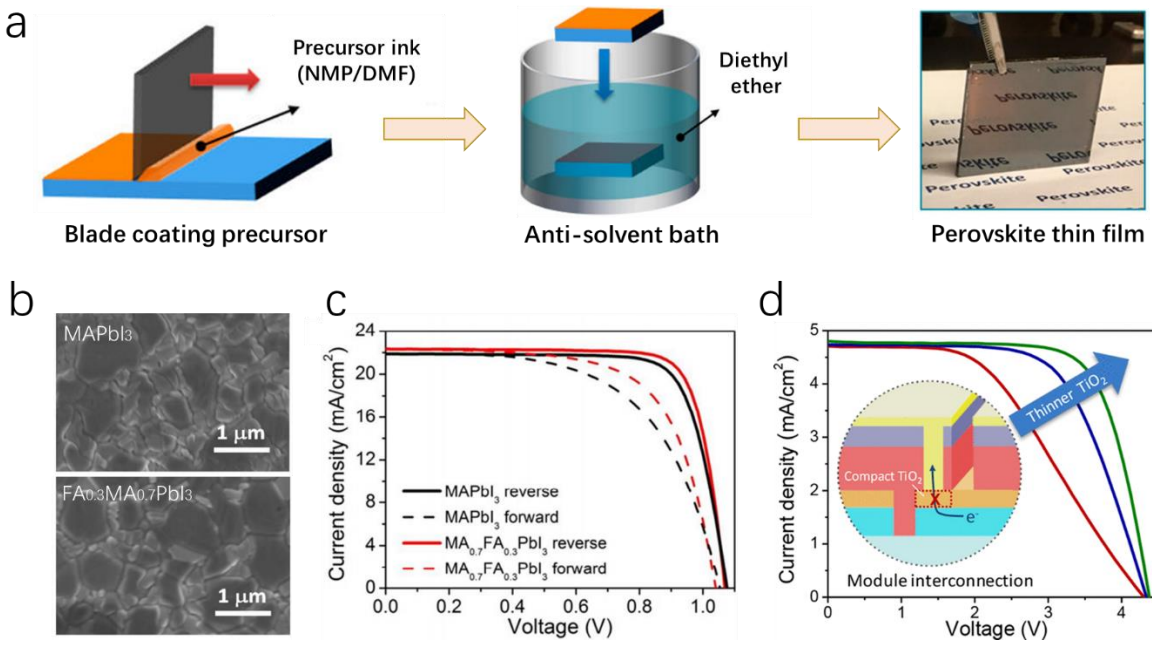

Figure 8. (**a**) Schematic illustration of perovskite film prepared by blade-coating with assistance of antisolvent extraction. (**b**) Top-view SEM images of the perovskite $MAPbI_3$ (top) and $FA_{0.3}MA_{0.7}PbI_3$ (bottom) film prepared by anti-solvent quenching. (**c**) J-V curves of the perovskite solar cells with reverse and forward voltage scan. (**d**) J−V curves of four-cell series-connected $MAPbI_3$ solar modules as a function of TiO_2 film thickness ranging from ~10 to 100 nm. Reproduced with permission.[67] Copyright 2018, American Chemical Society.

In principle, antisolvent bathing imposes no limit on the substrate size and could be combined with blade-coating and other continuous coating methods (**Figure 8a**). Different from hot-casting and meniscus-assisted printing where the crystallization take place synchronously with the precursor deposition, crystallization based on antisolvent bathing is carried out after the completion of the precursor film deposition. Hence, to avoid the drying of the printed perovskite precursor film before immersing it into the antisolvent bath, it is important that either an ultrafast transfer or a wide processing window can be achieved to ensure reproducible and scalable fabrication of PSCs. In practice, it would be intriguing to formulate a perovskite ink by means of solvent and additive engineering to keep the printed precursor film wet over a long period after deposition. Previous studies have shown that a mixed solvent containing GBL, DMSO and NMP leads to a longer evaporation time compared to single DMF for the perovskite precursor solutions, owing to the low saturated

vapor pressure and the formation of an adduct between DMSO and PbI_2.[6] In 2017, Yang *et al.* reported on the development of a slow-drying perovskite precursor to ensure antisolvent extraction in a scalable blade-coating deposition.[68] Using a solvent mixture of N-methyl-2-pyrrolidone (NMP) and DMF with a volume ratio of 9:8, a wide process window up to 8 min is achieved. Methylammonium chloride (MACl) is incorporated into the perovskite precursor, which is beneficial for the recrystallization of perovskite films to form dense and large grains with enhanced crystallinity. The combination of solvent and additive engineering enables blade coating of uniform and pinhole-free perovskite films of different compositions by antisolvent bath (**Figure 8b**).[67] Photovoltaic devices with an active area of 0.12 cm^2 show efficiencies of 18.08% and 18.96% for the light absorber of $MAPbI_3$ and $FA_{0.3}MA_{0.7}PbI_3$, respectively. Moreover, a series-connected four-cell module with an active area of 10.36 cm^2 yields a stabilized PCE of 15.6%.

Antisolvent bathing has also been implemented in other scalable printing methods. In 2018, Whitaker *et al.* applied the antisolvent extraction method to crystallize perovskite precursor films deposited by slot-die coating and demonstrated almost identical photovoltaic performance to those prepared by spin-coating and blading.[69] Employing the same material system, they further fabricated a 15.6% efficiency perovskite module by antisolvent bathing through the optimization of the interconnections.[67]

5.5 Gas quenching

Gas quenching relies on convection forces to quickly extract the coordinating solvent from the precursor film and induce nucleation and crystal growth. In this process, gas flow rate and gas temperature are the two important parameters in delivering high-quality thin films of perovskites. In addition, the solvent composition that allowing the formation of stable intermediate phase is another important consideration. Early in 2014, Huang et al. reported, for the first time, the gas-blowing method for the preparation of $MAPbI_3$ films by spin-

coating.[70] During substrate rotation, dry argon gas with a pressure of 40 psi is blown over the surface of the precursor solution to promote evaporation of the solvent, thereby leading to rapid supersaturation of the film. The perovskite film prepared by gas quenching shows a dense and compact morphology without pinholes after thermal annealing, whereas the films prepared without gas quenching exhibit a dendritic grain morphology. Later in 2016, Snaith and coworkers extended gas quenching as a general technique to produce smooth pinhole-free perovskite films of a wide variety of material compositions.[71] They found that the addition of DMSO to a DMF-based precursor plays a key role in achieving dense and smooth perovskite films due to the formation of an intermediate perovskite precursor-DMSO complex. As a result, retarded crystal growth is realized, analogous to the antisolvent quenching method. Similar to antisolvent extraction, the timing of gas-blowing during spinning should be carefully optimized depending on the material composition and solvent systems.

Gas quenching was later developed for depositing perovskite films by scalable methods. In 2015, Di Carlo and coworkers used the concept to fabricate PSCs via two-step blade coating.[72] To obtain uniform and smooth perovskite layers, an airflow system was introduced during blade coating of PbI_2, resulting in a compact film morphology. The conversion of $MAPbI_3$ perovskite is carried out by immersing the resultant PbI_2 in a MAI bath. An efficiency of 13.3% is obtained for small-size blade coated perovskite devices. Perovskite modules with active areas of 10.1 and 100 cm^2 deliver efficiencies of 10.3% and 4.3%, respectively. Also in 2015, Vak *et al.* reported the application of a 3D slot-die coater for the two-step sequential deposition of perovskite films.[73] They attach a second slot-die head behind the first slot-die head, where the second head is connected to high-pressure nitrogen which is used to quickly dry the PbI_2 by blowing nitrogen gas. To improve the uniformity of the PbI_2 layer, the slot-die coated PbI_2 has to be stored in an enclosed container. The resulting

PbI_2 layer exhibits micro crack structure which enables a much faster conversion to perovskite when it reacts with the slot-die coated MAI solution. Careful optimization of the coating speed and substrate temperature yields a PCE of 11.96% for fully slot-die coated perovskite solar cells. Using an air blade to assist solvent drying, the gas quenching method was also applied for one-step slot-die coating of mixed lead halide perovskites.[18] In addition, hot gas quenching was developed to crystallize $MAPbI_3$ films prepared by one-step slot-die printing of a nonstoichiometric precursor of lead acetate and MAI.[53]

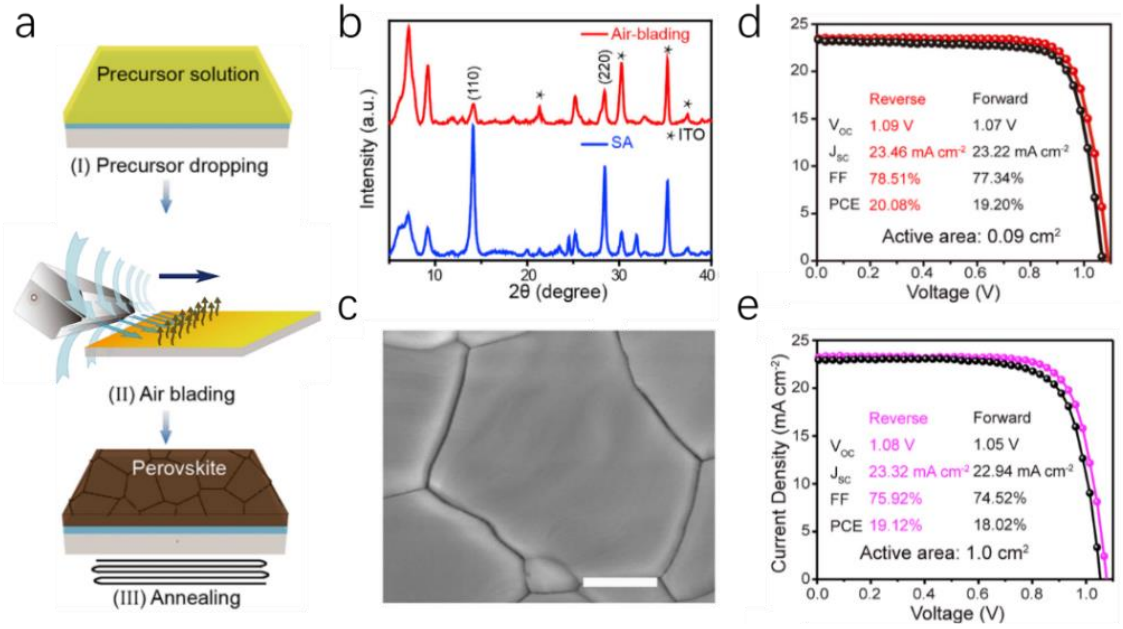

Figure 9. (**a**) Schematic diagram of perovskite film deposition by air-blading process. (**b**) X-ray diffraction (XRD) patterns of the air-bladed $MAPbI_3$ intermediate films obtained with gas-quenching and antisolvent quenching. (**c**) Top-view SEM image of air-bladed $MAPbI_3$ film with 5% $Pb(SCN)_2$ additive. Scale bar, 500 nm. J–V characteristics of the best-performing device with illumination-exposure area of 0.09 cm^2 (**d**) and 1.0 cm^2 (**d**). Reproduced with permission.[74] Copyright 2018, Elsevier.

In 2018, Hu and coworkers developed an elegant air-blading technique which is capable of spreading precursor solution and, simultaneously, inducing solvent evaporation (**Figure 9a**).[74] They found that air blading of a perovskite precursor solution at room temperature produces an intermediate adduct consisting of $(MA)_2[(PbI_3)_2PbI_2]\cdot 2DMSO)$, which is analogous to the antisolvent extraction method (**Figure 9b**). In their air-blading process, the

thickness of the perovskite films can be tailored by controlling the pressure of the input N_2 flow. In addition, a small amount of lead thiocyanate ($Pb(SCN)_2$) is incorporated as additive to facilitate the growth of uniform and compact perovskite film with large grains size (> 2 um) and long carrier lifetime (**Figure 9c**).[75] Perovskite solar devices prepared by air blading at a pressure of 0.3 MPa yield high efficiencies of 20.08% and 19.12% for active areas of 0.09 and 1.0 cm^2, respectively (**Figure 9d and 9e**).

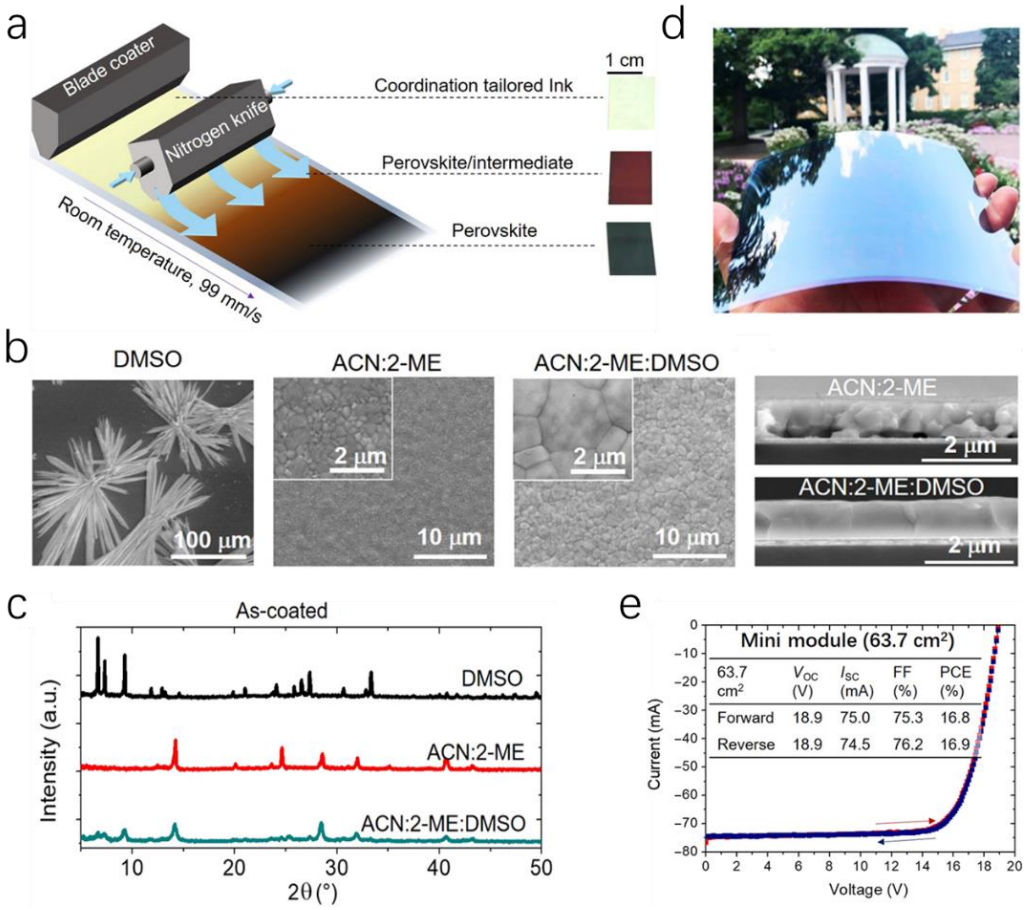

Figure 10. (**a**) Schematic illustration of gas-quenching-assisted blade coating of perovskite films. Photograph images are as-coated ink, intermediate film, and crystalline perovskite. (**b**) Top-view and cross-sectional SEM images of perovskite films prepared with different solvent or solvent mixtures. (**c**) XRD spectra of as-coated perovskite films from different solvent or solvent mixtures. (**d**) Digital image of a gas-quenching prepared perovskite film on 15×15 cm^2 flexible substrate. (**e**) Current–voltage curve of the champion perovskite module with an active area of 63.7 cm^2. Reproduced with permission.[76] Copyright 2019, American Association for the Advancement of Science.

Through tailoring the solvent coordination capability, in 2019 Huang and coworkers extended the gas quenching technology for blade coating perovskite films at an ultra-high speed of 99 mm/s (**Figure 10a**).[76] They found that processing from the coordinating solvent of pure DMSO results in dendritic crystals (**Figure 10b**), owing to the formation of intermediate phases composed of PbI_2-MAI-DMSO which are stable at room temperature (**Figure 10c**). On the other hand, processing from noncoordinating solvents (i.e. acetonitrile) enables to skip the generation of the intermediate film, which eventually leads to small crystal grains with poor physical contact with the interface layer beneath (**Figure 10b**). The utilization of coordinating and noncoordinating solvent mixture produces dense perovskite films with large crystals, owing to the slow release of coordinating solvent during film formation. The decoupling of the precursor coating and temperature-induced crystallization ensures high reproducibility, which is demonstrated by fabricating a large-area perovskite film on a flexible substrate (**Figure 10d**) and a mini module (63.7 cm^2) showing a certified efficiency of 16.4% (**Figure 10e**). Very recently, gas-quenching was applied to fabricate flexible perovskite devices by blade-coating. Small-sized (0.08 cm^2) devices and large-area (42.9 cm^2) flexible modules fabricated on Corning Willow Ultrathin Glass show high efficiencies of 19.72% and 15.86%, respectively.[77] Given the general application of the air-blading coating in industrial,[78, 79] it is anticipated that the air-blading can be applied to up-scaling perovskite thin films by continuous roll-to-roll manufacturing.

5.6 Vacuum quenching

Vacuum quenching relies on changes in pressure to remove the coordinating solvent of the printed precursor films and initiate nucleation by reaching supersaturation. Similar to solvent bath extraction and gas quenching strategies, one distinct advantage of vacuum quenching is that the precursor solution deposition and thermally induced crystallization can be effectively decoupled. In 2015, Xie *et al.* reported a vacuum-assisted thermal annealing

process to modulate the composition and morphology of $MAPbI_3$ films.[80] They found that the implementation of a vacuum can effectively remove the byproduct of MACl generated from a perovskite precursor consisting of CH_3NH_3I and $PbCl_2$ during thermal annealing, which gives rise to composition-pure and pore-free $MAPbI_3$ films. Vacuum assisted thermal annealing was later applied to crystallize perovskite films prepared by inkjet printing.[81] In the vacuum quenching processes, the vacuum degree and vacuum duration are the two determinative parameters that should be taken into account.[82] A year later in 2016, a major advance was realized by developing a vacuum flash-assisted solution processing to produce uniform and high-crystalline perovskite thin films.[83] Subjecting the freshly spin-coated precursor film to a high vacuum enables sudden removal of solvent residual in a controlled manner. As a result, rapid crystallization of a fibrous complex consisting of a Lewis acid–base type adduct is obtained, which is converted to crystalline perovskite with subsequent thermal annealing. Solar devices with an aperture area of 1 cm^2 prepared by vacuum flash-assisted processing delivers a certified efficiency approaching 20%.[83]

In an early stage, the vacuum quenching technique was primarily pursued for perovskite deposition by spin coating with the aspiration of replacing antisolvent dripping.[82-87] A significant advance was achieved in 2019 by extending the vacuum quenching strategy to large-area deposition of high-quality perovskite films by blade coating.[88-91] In a two-step sequential approach, a vacuum apparatus is deployed to extract the superfluous solvent of the freshly deposited inorganic component PbI_2 (**Figure 11a**).[88] It is shown that the choice of solvent and the subjection to a mild vacuum are the two most important factors to obtain homogenous lead iodide (PbI_2) films. Depositing PbI_2 from single solvent of DMF leads to large haze with obvious coffee rings, owing to the fast evaporation of the solvent DMF because of its high vapor pressure (2.70 mmHg at 20 °C) (**Figure 11b**). On the other hand, blade-coating PbI_2 from a binary solvent mixture of DMSO and DMF produces a more

homogenous film, but the naturally dried PbI_2 exhibits needle-like crystals, mainly owing to the preferred crystals growth of the PbI_2-DMSO adduct during slow solvent evaporation (**Figure 11c**). In contrast, deploying a vacuum extraction on the freshly coated PbI_2 precursor film processed from 9:1 DMF/DMSO solvent allows rapid removal of the excess solvent, which results in a solid PbI_2 layer with smooth and shiny appearance over the entire substrate (**Figure 11d**). More significantly, the resulting PbI_2 film exhibits a mesoporous structure, which is highly desired for perovskite conversion via an insertion reaction with the organic salt MAI. As a result, homogenous and compact $MAPbI_3$ films are obtained by coating a solution MAI on top of PbI_2 at a mild temperature of 50 °C.

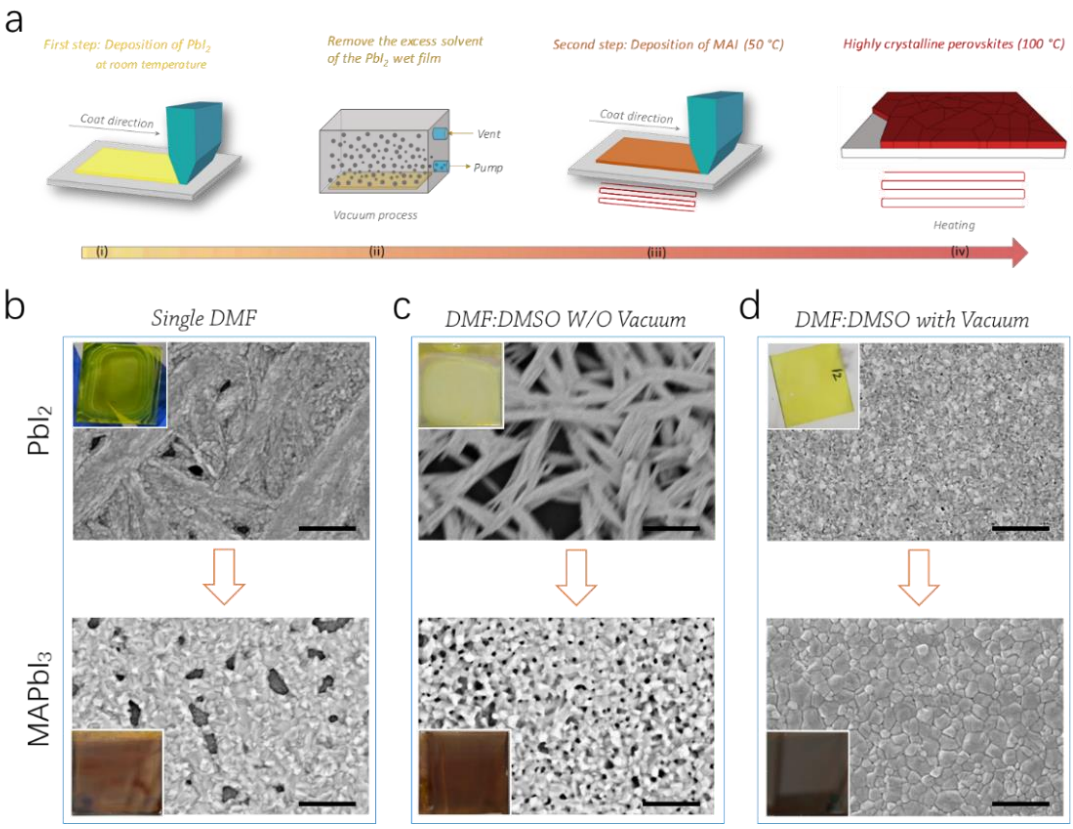

Figure 11. (**a**) Schematic illustration of the two-step sequential deposition of perovskite film via blade coating. (**b**) SEM image of the blade-deposited PbI_2 film processed from pure DMF (top) and the converted perovskite film (bottom). SEM image of the blade-deposited PbI_2 film processed from solvent mixture of DMF:DMSO without (**c**) and with (**d**) vacuum quenching process, and their converted perovskite films (bottom). The insets in (b)–(d) are the corresponding digital photographs of the prepared PbI_2 (top) and perovskite films (bottom). The scale bars in all images are 1 µm. Reproduced with permission.[88] Copyright 2019, Wiley-VCH.

In 2019, a generalized one-step approach based on vacuum-quenching was developed, which allows to prepare dense and uniform perovskite films over large areas (**Figure 12a**).[89] Subjecting the freshly coated precursor wet film to a mild vacuum of 1000 Pa produces an intermediate film composed of a mixture of crystalline perovskite and intermediate phase with a molecular structure of $MA_2Pb_3I_8 \cdot 2DMSO$. It is found that incorporating processing additives (MACl, MASCN, KSCN etc.) to the precursor solution facilitates the growth of perovskite crystals during the vacuum process (**Figure 12b** and **12c**). Homogenous large-area perovskite films with high specular reflection and low-haze transmittance are obtained by applying thermal annealing to the vacuum-processed intermediate films (**Figure 12d**). Inverted perovskite devices prepared by one-step vacuum quenching deliver a PCE over 18% with a high FF of 80% (**Figure 12e**). A large-area solar module is also fabricated (**Figure 12f**), demonstrating the scalability of the technology. Furthermore, solar cells based on three perovskite material compositions with different bandgaps were fabricated (**Figure 12g**), illustrating the general applicability of the one-step vacuum quenching technology.

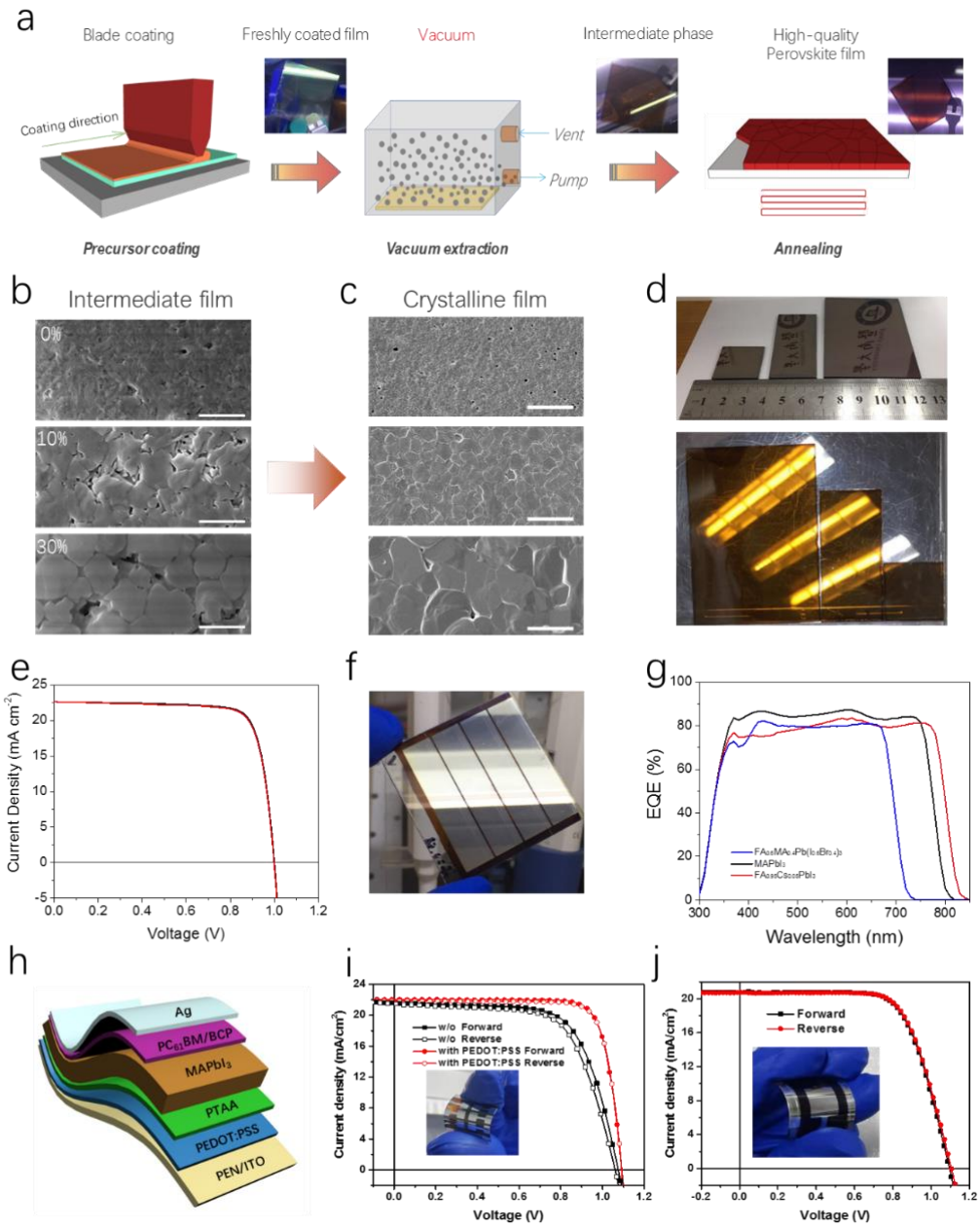

Figure 12. (**a**) Schematic illustration of the one-step deposition of perovskite films via blade coating. (**b**) SEM images of intermediate films obtained by vacuum quenching, which are processed without (top), with 10% (middle), and 30% (bottom) MACl; Scale bars are 1 μm. (**c**) XRD spectra of the corresponding intermediate films shown in (**b**). (**d**) Digital images of the $MAPbI_3$ films with dimensions of 2.5×2.5 cm^2, 2.5×5 cm^2 and 5.5×7 cm^2. (**e**) J–V curves of the best-performing $MAPbI_3$ (10% MACl) device. (**f**) Digital photograph of a blade-coated $MAPbI_3$ module with active area of 10.08 cm^2. (**g**) EQE spectra of the $FA_{0.6}MA_{0.4}Pb(_{I0.6}Br_{0.4})_3$, $MAPbI_3$ and $FA_{0.95}Cs_{0.05}PbI_3$ perovskite solar cells. (**h**) Schematic structure of a flexible perovskite solar cell. (**i**) J–V curves of the best-performing small-size (0.1 cm2) flexible cells deposited on different hole transport layers. Inset shows the photo of the device. (**j**) J–V curves of the best-performing large-size (1 cm^2) flexible PSC. Inset shows the photo of the device. (a)–(g) Reproduced with permission.[89] Copyright 2019, Wiley-VCH. (h)–(j) Reproduced with permission.[92] Copyright 2020, Wiley-VCH.

In the follow-up works, the vacuum quenching protocol was extended to scalable fabrication of low-bandgap tin–lead (Sn–Pb) mixed perovskites by blade coating.[93, 94] High-quality thin films of Sn–Pb perovskites with different bandgaps are facilely prepared by subjecting the freshly coated precursor films to a vacuum, followed by a thermal annealing process.[93] Solar cells based on vacuum-quenching processed $(MAPbI_3)_{0.75}(FASnI_3)_{0.25}$ deliver high efficiencies over 17%,[94] comparable to those prepared by antisolvent spin coating. In a very recent work, the vacuum quenching approach was used to fabricate flexible perovskite solar cells on polymer substrate by blade coating (**Figure 12h**).[92] Morphology engineering in combination with interface design successfully addresses the two major challenges: depositing high-quality perovskite layers on polymer substrates with high roughness and the inefficient charge extraction due to the energetic mismatch at interface. In particular, the rationally designed double hole transport layers comprised of "poly(3,4–ethylenedioxythiophene):poly(styrenesulfonate)/poly[bis(4-phenyl)(2,4,6-trimethylphenyl)amine]" forms a cascaded energy level alignment with the adjacent layers of polyethylene naphthalate/indium tin oxide and perovskite, which ultimately gives rise to enhanced spectral response as well as remarkably improved fill factors. The champion small-size flexible perovskite cells prepared by vacuum-assisted blade-coating delivers an efficiency as high as 19.41% with a high FF of 81% (**Figure 12i**). In addition, a large-size flexible device with an active area of 1 cm^2 yields an efficiency of 16.61% (**Figure 12j**), which is comparable to the flexible PSCs prepared by spin-coating.[95, 96]

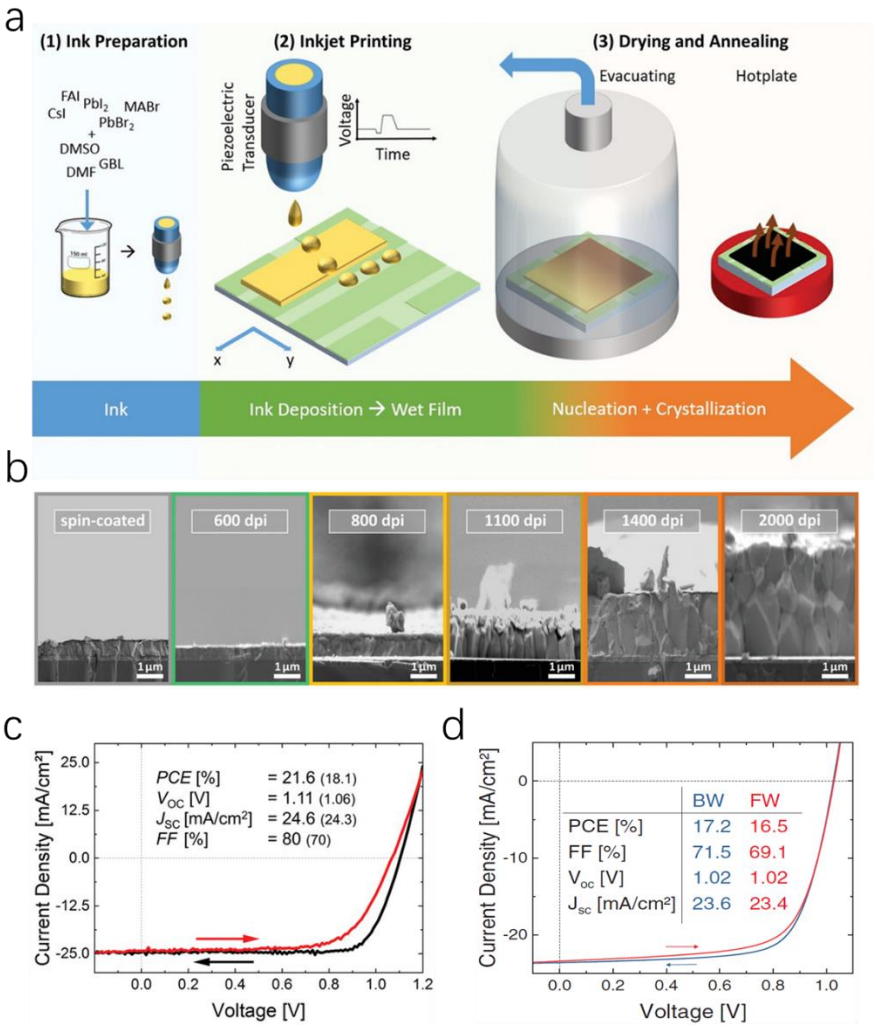

Figure 13. (**a**) Schematic illustration of the inkjet printing of triple-cation perovskite films based on vacuum quenching. (**b**) Cross-sectional SEM images of the perovskite films inkjet-printed with different droplet resolutions. A spin-coated sample is shown as well. (**c**) J–V characteristics of a PSC with inkjet-printed triple-cation perovskite layer. (**d**) J–V curves of an all-inkjet-printed perovskite device. Reproduced with permission.[20] Copyright 2020, Wiley-VCH.

In addition to blade coating, vacuum quenching has also been applied for the fabrication of triple-cation perovskite layers by inkjet printing and spray coating (**Figure 13a**).[20, 97] It is shown that the thickness of perovskite films can be easily controlled by adjusting the density of the ink droplets. Perovskite layers with thicknesses ranging from 400 nm up to 4 µm can be facilely prepared by inkjet printing with a droplet resolution from 600 to 2000 dots per inch (**Figure 13b**). Solar devices based on the vacuum quenching assisted inkjet printing

yield a champion efficiency of 21.6% from the reverse scan (**Figure 13c**). In a very recent report, a perovskite solar cell which was completely inkjet printed with exception of the two charge-collecting electrodes was fabricated, giving an efficiency of 17.2% (**Figure 13d**).[98]

5.7 Radiative annealing

Irradiation offers a rapid and contactless approach of heating target materials, which enables not only the photon energy to be effectively absorbed in the active layer, but also in the underlying transparent conductive contact.[99] In contrast to the highly energy consuming thermal processes, irradiative annealing allows significant reduction of the manufacture cost, owing to their short processing time and more efficient energy utilization. In 2015, Troughton et al. developed a rapid irradiation annealing process to crystallize spin-coated $MAPbI_3$ on an aluminium oxide scaffold. The crystallization time is significantly reduced from 45 min of annealing in a conventional oven to 2.5 s by near infrared radiation without significant performance losses.[100] Switching to an intensive photonic flash sintering technique, the processing time was further reduced to 1.15 ms. Unfortunately, the prepared perovskite films exhibit incomplete surface coverage and, thus lower device performance compared to the conventional thermally annealed devices.[101]

A notable advance was achieved in 2016 by Pool et al., who applied radiative thermal annealing to formamidinium lead iodide ($FAPbI_3$) and prepared solar cells with photovoltaic performance slightly outperforming the devices prepared by hotplate annealing.[102] Similarly, ultraviolet light-emitting diodes (LEDs) have been utilized for annealing perovskite which offers the advantage of layer-specific annealing, because the LED light source is able to provide a specific UV wavelength for maximum light absorption in the target layer.[103] Recently, ultrafast laser scribing has been exploited as an effective technique to anneal perovskite films. By tuning the laser scanning parameters, such as laser wavelength, scanning speed and output power, perovskite films with larger crystalline grains compared

to thermally annealed samples are obtained. Solar devices based on laser annealed $MAPbI_3$ photoactive layers exhibit an efficiency of up to 20%.[104] However, it has to be noted that, prior to subjection to radiative laser annealing, an intermediate film has to be created by antisolvent quenching during spin-coating, which limits its potential for upscaling.[102, 103 104]

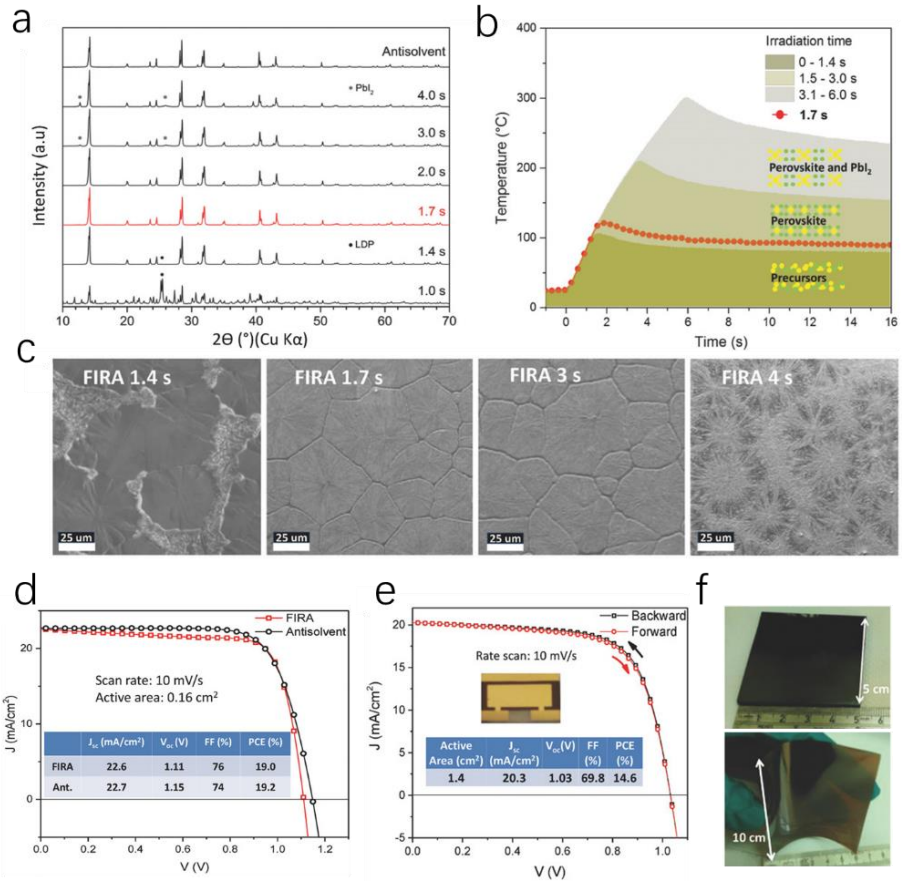

Figure 14. (**a**) XRD patterns of perovskite layer prepared with different infrared irradiation time. (**b**) Temperature profiles of the substrate for different FIRA annealing pulse lengths. (**c**) SEM images of FIRA-annealed perovskite films for four annealing times, scale bar: 25 µm. (**d**) J–V curves of the small-size (0.16 cm^2) champion devices and the corresponding photovoltaic parameters. (**e**) J–V curves of the best-performing large-size (1.4 cm^2) solar cell. (**f**) Pictures of large-area perovskite films (100 cm^2) made by FIRA on rigid (top) and flexible substrates (bottom). Reproduced with permission.[105] Copyright 2018, Wiley-VCH.

In order to realize upscaling of the technology, it is of great significance that the antisolvent dripping step commonly involved in perovskite deposition by spin-coating can be avoided.

In 2018, Sanchez et al. reported a flash infrared annealing (FIRA) approach which allows to skip the antisolvent quenching involved in spin-coating.[105] They found that the crystal structure and morphology of the perovskite films are closely correlated with the FIRA pulse duration (**Figure 14a**). A short irradiation time of 1.0 s produces 3D $MAPbI_3$ film along with larger contribution of low-dimensional perovskites (**Figure 14c**). An irradiation time of 1.7–2.0 s results in large and pinhole-free crystalline domains with XRD patterns resembling the antisolvent sample. Further increasing the irradiation time leads to the decomposition of $MAPbI_3$ into PbI_2. The optimal pulse duration is identified to be in the range of 1.5–3 s, which enables the formation of phase-pure perovskite films (**Figure 14b**). Solar cells with active areas of 0.16 cm^2 and 1.4 cm^2 processed with 1.7 s irradiation time $MAPbI_3$ give efficiencies of 19.0% and 14.6%, respectively (**Figure 14d and 14e**). The practical application of the FIRA for upscaling is supported by manufacturing uniform large-area perovskite films (100 cm^2) on both glass and polymer substrates (**Figure 14f**). A detailed study giving comparisons with the common lab-scale antisolvent method suggests that the flash infrared annealing is potentially a cost-effective method with a low environmental impact for the fabrication of highly efficient perovskite solar cells.[106]

6. Morphology optimization in scalable coated perovskite films

6.1 Additive engineering

In the previous section, we have presented a detailed discussion of the several crystallization technologies capable of depositing photovoltaic perovskite films by scalable methods. In essence, these technologies rely on the fast removal of the precursor solvent, thereby inducing rapid supersaturation. In addition, a consensus reached on the growth of perovskite thin films is that the nucleation and crystal growth are also heavily correlated with the solution chemistry of precursors. A large number of studies has shown that the morphology

of perovskite films can be regulated by varying the chemical composition and/or by introducing additives to the precursor solution.[37, 50, 87, 89, 92, 107, 108]

In the early stages of perovskite research, chloride-containing precursors ($PbCl_2$ and MAI) were commonly used to produce perovskite layers with better coverage and larger grain sizes than those obtained from a stoichiometric precursor (PbI_2 and MAI).[28, 109] Other typical chloride additives such as MACl, formamidinium chloride, NH_4Cl and $Pb(SCN)_2$ are also capable of regulating the morphology of perovskite films.[89, 110-113] In addition, the orientation and crystallinity of the perovskite films can also be effectively tailored by incorporating these additives.[68, 89] It has been revealed that the as-spun film processed from chloride-containing precursors consists of crystalline MA_2PbI_3Cl,[114, 115] coexisting with amorphous MACl. The generated intermediate film is less crystalline than the film deposited directly from the stoichiometric precursor. In addition, the presence of MACl impedes the transformation of precursor into perovskite.[114] Upon thermal annealing, the slow evaporation of MACl acts as a self-regulating mechanism to retard the conversion, resulting in a perovskite film with dense coverage and improved crystal quality. Although these additives are initially used in spin-coated perovskite devices, they are also applicable in scalable coating methods. For example, MACl/NH_4Cl has been demonstrated as effective additive in modulating crystal morphology of perovskite films deposited by scalable methods with assistance of hot-casting,[37] solvent-extraction,[68] vacuum quenching,[89, 92] and gas-quenching.[77] Other surfactant-based additives are shown to have great impact on ink drying kinetics which enables high-speed deposition of perovskite photovoltaic layers.[50]

6.2 Lewis acid–base adduct approach

Lewis acids and bases are described by the Lewis theory of acid-base reactions as electron-pair acceptors and electron pair donors, respectively. A Lewis base can donate a pair of electrons to a Lewis acid to form a product containing a coordinating covalent bond. In

perovskite precursors, Pb^{2+} halides are strong Lewis acids that can readily form adducts with Lewis-basic solvents or additives.[116, 117] The formation of Lewis acid–base adducts in the precursor solution enhances the solubility of lead halides.[118] Moreover, the Lewis acid–base adducts have enabled the development of the adduct approach, utilizing the adduct film as an intermediate phase to control the crystallization kinetics of perovskite films. Through the selection of Lewis bases with different basicity, the nucleation and crystal growth can be effectively modulated. In this regard, the Lewis acid–base approach can be used to improve the morphology of perovskite thin films. For example, the addition of DMSO or thiourea to a precursor solution of PbI_2 and MAI in DMF leads to the formation of a Lewis acid–base adduct, [117, 119] and the morphology of the resultant thin film is greatly improved compared with the film prepared from the pristine precursor solution.[92] In addition to DMSO, other Lewis-basic solvents, such as pyridine and NMP, can be used for adduct formation.[120] Other examples of Lewis-basic additives with the ability to modify perovskite thin-film morphologies are urea,[121, 122] thiocyanate and thiosemicarbazide.[123] These additives have been demonstrated to improve the morphology of perovskite thin films as well as passivate the defect states due to the strong bonding between the under-coordinated Pb^{2+} and the Lewis basic molecules,[124, 125] which are beneficial for large-area fabrication of perovskite films by scalable methods.

6.3 Post-growth approach

In perovskite solar devices, the thickness of light absorber layers is typically in the range of 300−600 nm. With such a thin layer, film uniformity and complete surface coverage are the two essential factors to the production yield of large-area perovskite modules. Even with myriad strategies addressing crystal morphology, perovskite deposition is still fundamentally sensitive to the processing conditions. The variation of processing parameters and changes even on a small scale in the local atmosphere can result in inferior device

performance due to the formation of pinholes and structural defects. To eliminate the structural defects in the prepared perovskite films, several post-annealing treatments have been developed, which can increase the process reliability for reproducible fabrication of large-area perovskite modules.

Solvent vapor annealing of perovskite films in a controlled environment has been demonstrated as an effective technique to enhance the grain size and crystallinity and to remove local pinholes. Several solvents have shown an efficient Ostwald ripening effect to heal the structural defects in perovskite thin films and resulted in enhanced solar cell performance. For example, Huang and coauthors reported the use of DMF vapor annealing to increase the grain size and improve the electronic quality of perovskite films.[126] Other solvents including water, alcohols, DMSO, GBL or combinations of them have been utilized for solvent vapor annealing.[127-129]

An Ostwald ripening approach enabled by coating a solution of ammonium halide has also been demonstrated to heal the structural defects in perovskite thin films. The ripening process removes pinholes and increases the grain size and crystallinity of the perovskite film. For example, $MAPbI_3$ films treated with a diluted MABr solution (2 mg ml^{-1}), followed by a brief annealing at 150 °C exhibit a more uniform and compact morphology with larger crystal grains.[130] It is also reported that a capping layer consisting of a material with a larger bandgap can be formed by coating a solution of guanidinium bromide, which is capable of reducing nonradiative recombination of the solar devices due to defect passivation on the perovskite surface.[131] As a result, a V_{OC} gain up to 100 mV is realized without sacrificing photocurrent.

6.4 Impact of interface layer

It is well documented that the surface energy of the charge transporting layers significantly influences the solution processability and morphology of the perovskite films. Hydrophobic

polymeric interfaces have shown to be beneficial for growing perovskite films with large crystal domains.[48] However, if the surface energy of the interface layers is significantly higher than that of the hydrophilic perovskite precursor solution, incomplete surface coverage of the perovskite films with numbers of pinholes can be formed. In sever circumstances, de-wettings are frequently observed due to the super-hydrophobic properties of the interfaces.[132] To bypass this limitation, surface modifications via oxygen plasma or ultraviolet-ozone treatment have been proposed to decrease the surface energy of the charge extracting layers,[133, 134] enabling to deposit dense and uniform perovskite layers on non-wetting interfaces. Nevertheless, one has to keep in mind that, the plasma-based surface modifications may negatively change the chemical structure of the materials, thereby altering the optoelectronic properties of the interface layers,[134] such as work function, transparency and mobility of the films. Prior to perovskite deposition, coating a thin layer of amphiphilic conjugated semiconducting polymer to lower down the surface energy of the hydrophobic interlayers offers another effective method.[132] Alternatively, physical modification by depositing a mesoporous insulating layer,[28, 49] acting as an inert scaffold, has been proved to be a viable approach allowing to deposit high-quality perovskite films without deteriorating the original optoelectronic properties of the interface layers. Not only does the surface energy of the interface layer influence the crystal morphology of perovskites, it was recently demonstrated that the wettability of the blade also has profound impact on the morphological properties of the scalable coated perovskite thin films.[135]

7. Summary and outlook

Perovskites solar cells have become a strong contender among photovoltaic technologies, rivaling the successful silicon-based solar panels and inorganic thin-film solar cells of cadmium telluride and copper indium gallium selenide. The intriguing efficiency advances achieved from low-temperature solution-processed devices have motivated the photovoltaic

community to devote resources for upscaling of the PSC technology. Notwithstanding, owing to the low entropy of the perovskite formation, the nucleation and subsequent crystal growth readily take place at room temperature during solution process. The low activation energy can lead to a rapid nucleation and crystal growth, making the control over the crystal morphology of scalable-coated the perovskite films elusive. In this review, starting with an in-depth analysis on the LaMer model, we conclude that controlling the crystallization kinetics by realizing a fast nucleation and retarded crystal growth is crucial to obtain uniform perovskite films with high surface coverage. Based on this guideline, we comprehensively analyze several emerging crystallization methods of great potential for the large-scale fabrication of perovskite thin film. Among them, hot-casting offers the most straightforward approach for high speed deposition of perovskite thin films, yet the simultaneous occurrence of nucleation and crystal growth generally requires experienced operation to achieve repeatable fabrication.[17, 37-39] As well, hot-casting may face challenges for roll-to-roll processing on flexible polymer substrates. Meniscus-assisted solution coating carried out at relatively low temperature alleviated the dilemma, but the coating speed represents a major limitation.[55] Derived from the classic antisolvent spin-coating, anti-solvent bathing is able to produce high-quality perovskite films by scalable methods.[68] However, recirculation of the antisolvent bath imposes a major technically concern for continuous high-throughput production. Enabling the decoupling of precursor solution deposition and the subsequent thermal annealing, gas quenching[74, 76] and vacuum quenching[88, 89] are promising protocols for reproducible fabrication of perovskite films. Apart from developing robust crystallization protocols for depositing high-quality perovskite absorber layers by scalable printing methods, there are several additional major challenges have to be addressed in order to realize practical application of the technology.

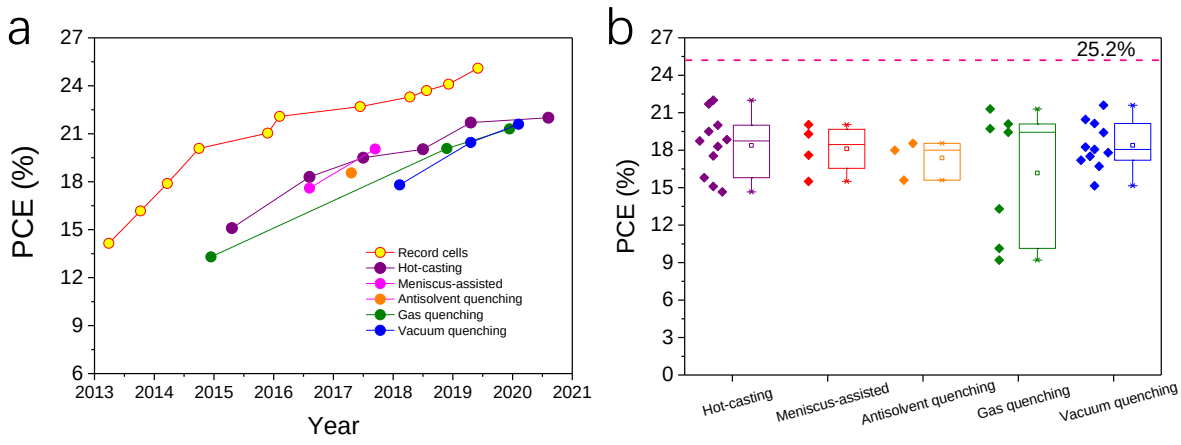

Figure 15. Efficiency evolution of PSCs taken from NERL chart and printed solar devices with perovskite layers prepared by scalable crystallization methods. The PCE of the scalable printed perovskite devices has gradually increased, yet a noticeable efficiency gap between the scalable printed devices and the record efficiency cells still remains.

1. Perovskite ink formulation

Currently, the large efficiency gap associated with the transition from laboratory devices to large-area modules is still noticeable (**Figure 15**), which represents one of the major obstacles towards commercial application.[136] The announcement of record efficiency is mainly realized on small-area devices fabricated by lab-scale spin-coating. Given the fundamental difference between the crystallization dynamics of the anti-solvent spin-coating (nucleates in second during anti-solvent washing) and the scalable coating (takes few tens of seconds for solvent removal), it is of imperative necessary to re-formulate the precursor ink specifically designed for scalable crystallization. In addition, developing new interface materials with outstanding optoelectronic properties and advanced module design and fabrication technique will accelerate closing the efficiency gap between lab-scale devices and large-area modules.

2. Addressing the stability

Stability is another critical issue in realizing the commercialization of the perovskite solar technology. MA-based perovskites are currently the most intensively investigated material, yet they show poor moisture and thermal stability due to the hydrophilicity and volatility of

MA^+. In comparison, mixed cations and mixed halide perovskites with better resistance to moisture and heat are more appealing for fabricating perovskite solar cells with long-term stability.[137, 138]

Dimensionality control can be a promising approach to enhance the stability of perovskite solar cells.[139] Recent studies indicated that, as compared to 3D perovskites, 2D perovskites possess notably higher ambient stability due to the moisture-resistance of the bulky organic cations.[140, 141] Combining the outstanding stability of 2D phase with the excellent photovoltaic properties of 3D perovskite offers a plausible way to simultaneously addressing the efficiency and stability of the devices. Incorporating a small amount of large-size ammonium cations into perovskite precursor, the prepared perovskites with mixed 2D/3D phases have shown great promise in reducing the degradation of the solar devices.[94, 141-143] Alternatively, constructing 2D/3D bilayer heterostructures via sequential layer-by-layer deposition[93, 144, 145] have received considerable attention due to their effectiveness in delivering high performance PSCs with significantly enhanced stability. Recently, spontaneous self-assembly of such a 2D/3D bilayer structure by one-step coating[118] has been demonstrated as another viable approach to improve the efficiency and stability. It should be noted that the defect states of the solution-processed perovskite layers are mainly located at the surface of the films. The formation of 2D perovskite thin layer on top of 3D crystals can effectively passivate the surface trap states, thereby significantly increasing the carrier lifetime, which is the key attributor for achieving high V_{OC}s.[93, 94, 118, 138]

Developing advanced packaging techniques such as depositing a water-resistant layer on top of perovskite solar cells may provide solutions to circumvent the environmental instability as well.[146] In addition, crystal crosslinking with modified molecules or blending hydrophobic additives into a perovskite will also improve the stability of PSCs towards commercialization.

3. All-inorganic perovskites

The current research interest is mainly focused on organic-inorganic perovskite composites that are capable of affording high efficiency devices. Nevertheless, it should be noted that all-inorganic perovskites are an important category of PSCs, mainly owing to their high thermal stability and rapid efficiency advances. Among them, $CsPbBr_3$ is relatively stable in ambient conditions, which is, however, not suitable for photovoltaic application due to its wide bandgap of 2.3 eV.[147, 148] The challenge to process Br/I mixed halide or $CsPbI_3$ all-inorganic perovskites with lower bandgaps mainly originates from their phase instability due to the easy formation of yellow δ-phase on the one hand,[149, 150] and the difficulty in controlling the crystal morphology of films due to the faster crystallization rate than the organic-inorganic counterparts on the other hand.[151] In this regard, we expect that slowing down the crystallization dynamics and stabilizing the black phase perovskites by rationally selecting processing additive would be a promising avenue to fabricate efficient all-inorganic PSCs by scalable methods. On the other hand, a recent study discovered a step-wise crystallization behavior in all-inorganic $CsPbI_2Br$, which was realized by optimizing the blade coating temperature during hot casting.[152]

4. Environmental impact

Lastly, it is worth noting that the highest performance PSCs with long-term stability still contain lead. Unfortunately, the toxicity of the heavy metal Pb and its solubility in water raises concerns with respect to the pollution to the human and environment, which hampers the acceptance of the technology and may conflict with legislative barriers. In this regard, more attention and research effort should be devoted to evaluating the environmental impact and to developing robust encapsulation techniques to prevent Pb leakage. In addition, simple and effective methods are supposed be developed to recycle the perovskite devices at the end of their lifetime.

Acknowledgements

The work was supported by the National Natural Science Foundation of China (Grant No. 61705090 and 62004089), Natural Science Foundation of Guangdong Province (2020A1515010853). C.J.B. gratefully acknowledges funding by the Deutsche Forschungsgemeinschaft (DFG, German Research Foundation) under the project numbers 182849149-SFB 953 and INST 90/917, INST 90/1093-1, financial support through the "Aufbruch Bayern" initiative of the state of Bavaria (EnCN and SFF) and the Bavarian Initiative "Solar Technologies go Hybrid" (SolTech). F.G. acknowledges funding from the Opening Project of Key Laboratory of Materials Processing and Mold, Zhengzhou University.

Conflict of Interest

The authors declare no conflict of interest.

References:

1. G. E. Eperon, S. D. Stranks, C. Menelaou, M. B. Johnston, L. M. Herz and H. J. Snaith, *Energ Environ Sci*, 2014, **7**, 982-988.
2. S. De Wolf, J. Holovsky, S. J. Moon, P. Loper, B. Niesen, M. Ledinsky, F. J. Haug, J. H. Yum and C. Ballif, *J Phys Chem Lett*, 2014, **5**, 1035-1039.
3. S. D. Stranks, G. E. Eperon, G. Grancini, C. Menelaou, M. J. P. Alcocer, T. Leijtens, L. M. Herz, A. Petrozza and H. J. Snaith, *Science*, 2013, **342**, 341-344.
4. A. Kojima, K. Teshima, Y. Shirai and T. Miyasaka, *J Am Chem Soc*, 2009, **131**, 6050-6051.
5. , https://www.nrel.gov/pv/cell-efficiency.html (accessed: July 2020).
6. N. J. Jeon, J. H. Noh, Y. C. Kim, W. S. Yang, S. Ryu and S. I. Seok, *Nat Mater*, 2014, **13**, 897-903.
7. J. Ramanujam, D. M. Bishop, T. K. Todorov, O. Gunawan, J. Rath, R. Nekovei, E. Artegiani and A. Romeo, *Prog Mater Sci*, 2020, **110**, 100619.
8. K. Shen, Y. Zhang, X. Wang, C. Ou, F. Guo, H. Zhu, C. Liu, Y. Gao, R. E. Schropp, Z. Li, X. Liu and Y. Mai, *Adv Sci*, 2020, 2001013.
9. N. J. Jeon, J. H. Noh, W. S. Yang, Y. C. Kim, S. Ryu, J. Seo and S. I. Seok, *Nature*, 2015, **517**, 476-480.
10. M. Graetzel, R. A. J. Janssen, D. B. Mitzi and E. H. Sargent, *Nature*, 2012, **488**, 304-312.
11. C. Sun, Z. H. Wu, H. L. Yip, H. Zhang, X. F. Jiang, Q. F. Xue, Z. C. Hu, Z. H. Hu, Y. Shen, M. K. Wang, F. Huang and Y. Cao, *Adv Energy Mater*, 2016, **6**, 1501534.
12. J. L. Hu, J. You, C. Peng, S. D. Qiu, W. X. He, C. H. Li, X. H. Liu, Y. H. Mai and F. Guo, *Sol Rrl*, 2020, **4**, 1900384.
13. Q. Jiang, Y. Zhao, X. W. Zhang, X. L. Yang, Y. Chen, Z. M. Chu, Q. F. Ye, X. X. Li, Z. G. Yin and J. B. You, *Nat Photonics*, 2019, **13**, 460-466.
14. F. Gao, Y. Zhao, X. W. Zhang and J. B. You, *Adv Energy Mater*, 2020, **10**, 1902650.
15. B. Chen, P. N. Rudd, S. Yang, Y. B. Yuan and J. S. Huang, *Chem Soc Rev*, 2019, **48**, 3842-3867.
16. G. Grancini, C. Roldan-Carmona, I. Zimmermann, E. Mosconi, X. Lee, D. Martineau, S. Narbey, F. Oswald, F. De Angelis, M. Graetzel and M. K. Nazeeruddin, *Nat Commun*, 2017, **8**, 15684.
17. Y. H. Deng, E. Peng, Y. C. Shao, Z. G. Xiao, Q. F. Dong and J. S. Huang, *Energ Environ Sci*, 2015, **8**, 1544-1550.
18. G. Cotella, J. Baker, D. Worsley, F. De Rossi, C. Pleydell-Pearce, M. Carnie and T. Watson, *Sol Energ Mat Sol C*, 2017, **159**, 362-369.
19. S. Das, B. Yang, G. Gu, P. C. Joshi, I. N. Ivanov, C. M. Rouleau, T. Aytug, D. B. Geohegan and K. Xiao, *ACS Photonics*, 2015, **2**, 680-686.
20. H. Eggers, F. Schackmar, T. Abzieher, Q. Sun, U. Lemmer, Y. Vaynzof, B. S. Richards, G. Hernandez-Sosa and U. W. Paetzold, *Adv Energy Mater*, 2020, **10**, 1903184.
21. S. Razza, S. Castro-Hermosa, A. Di Carlo and T. M. Brown, *APL Materials*, 2016, **4**.
22. G. E. Eperon, V. M. Burlakov, P. Docampo, A. Goriely and H. J. Snaith, *Adv Funct Mater*, 2014, **24**, 151-157.
23. W. S. Yang, B. W. Park, E. H. Jung, N. J. Jeon, Y. C. Kim, D. U. Lee, S. S. Shin, J. Seo, E. K. Kim, J. H. Noh and S. I. Seok, *Science*, 2017, **356**, 1376-1379.
24. J. A. Aguiar, S. Wozny, T. G. Holesinger, T. Aoki, M. K. Patel, M. J. Yang, J. J. Berry, M. Al-Jassim, W. L. Zhou and K. Zhu, *Energ Environ Sci*, 2016, **9**, 2372-2382.
25. J. W. Lee, D. K. Lee, D. N. Jeong and N. G. Park, *Adv Funct Mater*, 2019, **29**, 1807047.

26. Y. S. Jung, K. Hwang, Y. J. Heo, J. E. Kim, D. Vak and D. Y. Kim, *Adv Opt Mater*, 2018, **6**, 1701182.
27. Z. Li, T. R. Klein, D. H. Kim, M. J. Yang, J. J. Berry, M. F. A. M. van Hest and K. Zhu, *Nat Rev Mater*, 2018, **3**, 18017.
28. M. M. Lee, J. Teuscher, T. Miyasaka, T. N. Murakami and H. J. Snaith, *Science*, 2012, **338**, 643-647.
29. L. L. Gao, C. X. Li, C. J. Li and G. J. Yang, *J Mater Chem A*, 2017, **5**, 1548-1557.
30. J. Cao, X. J. Jing, J. Z. Yan, C. Y. Hu, R. H. Chen, J. Yin, J. Li and N. F. Zheng, *J Am Chem Soc*, 2016, **138**, 9919-9926.
31. J. Burschka, N. Pellet, S. J. Moon, R. Humphry-Baker, P. Gao, M. K. Nazeeruddin and M. Gratzel, *Nature*, 2013, **499**, 316-319.
32. J. H. Im, I. H. Jang, N. Pellet, M. Gratzel and N. G. Park, *Nat Nanotechnol*, 2014, **9**, 927-932.
33. H. N. Chen, *Adv Funct Mater*, 2017, **27**, 1605654.
34. Z. G. Xiao, C. Bi, Y. C. Shao, Q. F. Dong, Q. Wang, Y. B. Yuan, C. G. Wang, Y. L. Gao and J. S. Huang, *Energ Environ Sci*, 2014, **7**, 2619-2623.
35. Y. Z. Wu, A. Islam, X. D. Yang, C. J. Qin, J. Liu, K. Zhang, W. Q. Peng and L. Y. Han, *Energ Environ Sci*, 2014, **7**, 2934-2938.
36. W. Y. Nie, H. H. Tsai, R. Asadpour, J. C. Blancon, A. J. Neukirch, G. Gupta, J. J. Crochet, M. Chhowalla, S. Tretiak, M. A. Alam, H. L. Wang and A. D. Mohite, *Science*, 2015, **347**, 522-525.
37. S. Tang, Y. H. Deng, X. P. Zheng, Y. Bai, Y. J. Fang, Q. F. Dong, H. T. Wei and J. S. Huang, *Adv Energy Mater*, 2017, **7**, 1700302.
38. Y. H. Deng, Q. F. Dong, C. Bi, Y. B. Yuan and J. S. Huang, *Adv Energy Mater*, 2016, **6**, 1600372.
39. Z. B. Yang, C. C. Chueh, F. Zuo, J. H. Kim, P. W. Liang and A. K. Y. Jen, *Adv Energy Mater*, 2015, **5**, 1500328.
40. W. G. Kong, G. L. Wang, J. M. Zheng, H. Hu, H. Chen, Y. L. Li, M. M. Hu, X. Y. Zhou, C. Liu, B. N. Chandrashekar, A. Amini, J. B. Wang, B. M. Xu and C. Cheng, *Sol Rrl*, 2018, **2**, 1700214.
41. W. Q. Wu, Q. Wang, Y. J. Fang, Y. C. Shao, S. Tang, Y. H. Deng, H. D. Lu, Y. Liu, T. Li, Z. B. Yang, A. Gruverman and J. S. Huang, *Nat Commun*, 2018, **9**, 1625.
42. W. Q. Wu, Z. B. Yang, P. N. Rudd, Y. C. Shao, X. Z. Dai, H. T. Wei, J. J. Zhao, Y. J. Fang, Q. Wang, Y. Liu, Y. H. Deng, X. Xiao, Y. X. Feng and J. S. Huang, *Sci Adv*, 2019, **5**, eaav8925.
43. J. E. Kim, S. S. Kim, C. Zuo, M. Gao, D. Vak and D. Y. Kim, *Adv Funct Mater*, 2019, **29**, 1809194.
44. W. C. Chang, D. H. Lan, K. M. Lee, X. F. Wang and C. L. Liu, *Chemsuschem*, 2017, **10**, 1405-1412.
45. J. H. Heo, M. H. Lee, M. H. Jang and S. H. Im, *J Mater Chem A*, 2016, **4**, 17636-17642.
46. L. K. Huang, C. Li, X. X. Sun, R. Xu, Y. Y. Du, J. Ni, H. K. Cai, J. Li, Z. Y. Hu and J. J. Zhang, *Org Electron*, 2017, **40**, 13-23.
47. W. Q. Wu, P. N. Rudd, Q. Wang, Z. B. Yang and J. S. Huang, *Adv Mater*, 2020.
48. C. Bi, Q. Wang, Y. C. Shao, Y. B. Yuan, Z. G. Xiao and J. S. Huang, *Nat Commun*, 2015, **6**, 7747.
49. J. You, F. Guo, S. Qiu, W. He, C. Wang, X. Liu, W. Xu and Y. Mai, *J Energy Chem*, 2019, **38**, 192-198.

50. Y. H. Deng, X. P. Zheng, Y. Bai, Q. Wang, J. J. Zhao and J. S. Huang, *Nat Energy*, 2018, **3**, 560-566.
51. J. B. Li, R. Munir, Y. Y. Fan, T. Q. Niu, Y. C. Liu, Y. F. Zhong, Z. Yang, Y. S. Tian, B. Liu, J. Sun, D. M. Smilgies, S. Thoroddsen, A. Amassian, K. Zhao and S. Z. Liu, *Joule*, 2018, **2**, 1313-1330.
52. Y. F. Zhong, R. Munir, J. B. Li, M. C. Tang, M. R. Niazi, D. M. Smilgies, K. Zhao and A. Arnassian, *Acs Energy Lett*, 2018, **3**, 1078-1085.
53. Q. Hu, L. C. Zhao, J. Wu, K. Gao, D. Y. Luo, Y. F. Jiang, Z. Y. Zhang, C. H. Zhu, E. Schaible, A. Hexemer, C. Wang, Y. Liu, W. Zhang, M. Gratzel, F. Liu, T. P. Russell, R. Zhu and Q. H. Gong, *Nat Commun*, 2017, **8**, 15688.
54. H. C. Liao, P. J. Guo, C. P. Hsu, M. Lin, B. H. Wang, L. Zeng, W. Huang, C. M. M. Soe, W. F. Su, M. J. Bedzyk, M. R. Wasielewski, A. Facchetti, R. P. H. Chang, M. G. Kanatzidis and T. J. Marks, *Adv Energy Mater*, 2017, **7**, 1601660.
55. M. He, B. Li, X. Cui, B. B. Jiang, Y. J. He, Y. H. Chen, D. O'Neil, P. Szymanski, M. A. El-Sayed, J. S. Huang and Z. Q. Lin, *Nat Commun*, 2017, **8**, 16045.
56. F. Ye, H. Chen, F. X. Xie, W. T. Tang, M. S. Yin, J. J. He, E. B. Bi, Y. B. Wang, X. D. Yang and L. Y. Han, *Energ Environ Sci*, 2016, **9**, 2295-2301.
57. F. Ye, W. T. Tang, F. X. Xie, M. S. Yin, J. J. He, Y. B. Wang, H. Chen, Y. H. Qiang, X. D. Yang and L. Y. Han, *Adv Mater*, 2017, **29**, 1701440.
58. Z. M. Zhou, Z. W. Wang, Y. Y. Zhou, S. P. Pang, D. Wang, H. X. Xu, Z. H. Liu, N. P. Padture and G. L. Cui, *Angew Chem Int Edit*, 2015, **54**, 9705-9709.
59. H. Chen, F. Ye, W. T. Tang, J. J. He, M. S. Yin, Y. B. Wang, F. X. Xie, E. B. Bi, X. D. Yang, M. Gratzel and L. Y. Han, *Nature*, 2017, **550**, 92-+.
60. M. S. Yin, F. X. Xie, H. Chen, X. D. Yang, F. Ye, E. B. Bi, Y. Z. Wu, M. T. Cai and L. Y. Han, *J Mater Chem A*, 2016, **4**, 8548-8553.
61. M. D. Xiao, F. Z. Huang, W. C. Huang, Y. Dkhissi, Y. Zhu, J. Etheridge, A. Gray-Weale, U. Bach, Y. B. Cheng and L. Spiccia, *Angew Chem Int Edit*, 2014, **53**, 9898-9903.
62. Y. Yu, S. W. Yang, L. Lei, Q. P. Cao, J. Shao, S. Zhang and Y. Liu, *Acs Appl Mater Inter*, 2017, **9**, 3667-3676.
63. G. E. Eperon, T. Leijtens, K. A. Bush, R. Prasanna, T. Green, J. T. W. Wang, D. P. McMeekin, G. Volonakis, R. L. Milot, R. May, A. Palmstrom, D. J. Slotcavage, R. A. Belisle, J. B. Patel, E. S. Parrott, R. J. Sutton, W. Ma, F. Moghadam, B. Conings, A. Babayigit, H. G. Boyen, S. Bent, F. Giustino, L. M. Herz, M. B. Johnston, M. D. McGehee and H. J. Snaith, *Science*, 2016, **354**, 861-865.
64. E. Gu, X. Tang, S. Langner, P. Duchstein, Y. Zhao, I. Levchuk, V. Kalancha, T. Stubhan, J. Hauch, H. J. Egelhaaf, D. Zahn, A. Osvet and C. J. Brabec, *Joule*, 2020, https://doi.org/10.1016/j.joule.2020.1006.1013.
65. Y. Y. Zhou, M. J. Yang, W. W. Wu, A. L. Vasiliev, K. Zhu and N. P. Padture, *J Mater Chem A*, 2015, **3**, 8178-8184.
66. C. O. R. Quiroz, L. Levchuk, C. Bronnbauer, M. Salvador, K. Forberich, T. Heumuller, Y. Hou, P. Schweizer, E. Spiecker and C. J. Brabec, *J Mater Chem A*, 2015, **3**, 24071-24081.
67. M. J. Yang, D. H. Kim, T. R. Klein, Z. Li, M. O. Reese, B. J. T. de Villers, J. J. Berry, M. F. A. M. van Hest and K. Zhu, *Acs Energy Lett*, 2018, **3**, 322-328.
68. M. J. Yang, Z. Li, M. O. Reese, O. G. Reid, D. H. Kim, S. Siol, T. R. Klein, Y. Yan, J. J. Berry, M. F. A. M. van Hest and K. Zhu, *Nat Energy*, 2017, **2**, 17038.
69. J. B. Whitaker, D. H. Kim, B. W. Larson, F. Zhang, J. J. Berry, M. F. A. M. van Hest and K. Zhu, *Sustain Energ Fuels*, 2018, **2**, 2442-2449.

70. F. Z. Huang, Y. Dkhissi, W. C. Huang, M. D. Xiao, I. Benesperi, S. Rubanov, Y. Zhu, X. F. Lin, L. C. Jiang, Y. C. Zhou, A. Gray-Weale, J. Etheridge, C. R. McNeill, R. A. Caruso, U. Bach, L. Spiccia and Y. B. Cheng, *Nano Energy*, 2014, **10**, 10-18.
71. B. Conings, A. Babayigit, M. T. Klug, S. Bai, N. Gauquelin, N. Sakai, J. T. W. Wang, J. Verbeeck, H. G. Boyen and H. J. Snaith, *Adv Mater*, 2016, **28**, 10701-10709.
72. S. Razza, F. Di Giacomo, F. Matteocci, L. Cina, A. L. Palma, S. Casaluci, P. Cameron, A. D'Epifanio, S. Licoccia, A. Reale, T. M. Brown and A. Di Carlo, *J Power Sources*, 2015, **277**, 286-291.
73. K. Hwang, Y. S. Jung, Y. J. Heo, F. H. Scholes, S. E. Watkins, J. Subbiah, D. J. Jones, D. Y. Kim and D. Vak, *Adv Mater*, 2015, **27**, 1241-1247.
74. J. Ding, Q. W. Han, Q. Q. Ge, D. J. Xue, J. Y. Ma, B. Y. Zhao, Y. X. Chen, J. Liu, D. B. Mitzi and J. S. Hu, *Joule*, 2019, **3**, 402-416.
75. W. J. Ke, C. X. Xiao, C. L. Wang, B. Saparov, H. S. Duan, D. W. Zhao, Z. W. Xiao, P. Schulz, S. P. Harvey, W. Q. Liao, W. W. Meng, Y. Yu, A. J. Cimaroli, C. S. Jiang, K. Zhu, M. Al-Jassim, G. J. Fang, D. B. Mitzi and Y. F. Yan, *Adv Mater*, 2016, **28**, 5214-5221.
76. Y. H. Deng, C. H. Van Brackle, X. Z. Dai, J. J. Zhao, B. Chen and J. S. Huang, *Sci Adv*, 2019, **5**, eaax7537.
77. X. Z. Dai, Y. H. Deng, C. H. Van Brackle, S. S. Chen, P. N. Rudd, X. Xiao, Y. Lin, B. Chen and J. S. Huang, *Adv Energy Mater*, 2020, **10**, 1903108.
78. Z. L. Ouyang, M. J. Yang, J. B. Whitaker, D. W. Li and M. F. A. M. van Hest, *ACS Appl Energ Mater*, 2020, **3**, 3714-3720.
79. D. K. Lee, D. N. Jeong, T. K. Ahn and N. G. Park, *Acs Energy Lett*, 2019, **4**, 2393-2401.
80. F. X. Xie, D. Zhang, H. M. Su, X. G. Ren, K. S. Wong, M. Gratzel and W. C. H. Choy, *Acs Nano*, 2015, **9**, 639-646.
81. C. Liang, P. W. Li, H. Gu, Y. Q. Zhang, F. Y. Li, Y. L. Song, G. S. Shao, N. Mathews and G. C. Xing, *Sol Rrl*, 2018, **2**, 1700217.
82. B. Ding, Y. Li, S. Y. Huang, Q. Q. Chu, C. X. Li, C. J. Li and G. J. Yang, *J Mater Chem A*, 2017, **5**, 6840-6848.
83. X. Li, D. Q. Bi, C. Y. Yi, J. D. Decoppet, J. S. Luo, S. M. Zakeeruddin, A. Hagfeldt and M. Gratzel, *Science*, 2016, **353**, 58-62.
84. M. Y. Liu, Z. M. Chen, Q. F. Xue, S. H. Cheung, S. K. So, H. L. Yip and Y. Cao, *J Mater Chem A*, 2018, **6**, 16347-16354.
85. B. Ding, L. L. Gao, L. S. Liang, Q. Q. Chu, X. X. Song, Y. Li, G. J. Yang, B. Fan, M. K. Wang, C. X. Li and C. J. Li, *Acs Appl Mater Inter*, 2016, **8**, 20067-20073.
86. B. A. Nejand, I. M. Hossain, M. Jakoby, S. Moghadamzadeh, T. Abzieher, S. Gharibzadeh, J. A. Schwenzer, P. Nazari, F. Schackmar, D. Hauschild, L. Weinhardt, U. Lemmer, B. S. Richards, I. A. Howard and U. W. Paetzold, *Adv Energy Mater*, 2020, **10**, 1902583.
87. C. C. Wu, D. Wang, Y. Q. Zhang, F. D. Gu, C. H. Liu, N. Zhu, W. Luo, D. Han, X. Guo, B. Qu, S. F. Wang, Z. Q. Bian, Z. J. Chen and L. X. Xiao, *Adv Funct Mater*, 2019, **29**, 1902974.
88. F. Guo, W. X. He, S. D. Qiu, C. Wang, X. H. Liu, K. Forberich, C. J. Brabec and Y. H. Mai, *Adv Funct Mater*, 2019, **29**, 1900964.
89. F. Guo, S. Qiu, j. Hu, h. Wang, B. Cai, J. Li, X. Yuan, X. Liu, K. Forberich, C. J. Brabec and Y. Mai, *Adv Sci*, 2019, **6**, 1901067.
90. C. P. Li, J. Yin, R. H. Chen, X. D. Lv, X. X. Feng, Y. Y. Wu and J. Cao, *J Am Chem Soc*, 2019, **141**, 6345-6351.

91. Z. Y. Xu, R. H. Chen, Y. Z. Wu, R. Q. He, J. Yin, W. Lin, B. H. Wu, J. Li and N. F. Zheng, *J Mater Chem A*, 2019, **7**, 26849-26857.
92. Z. Wang, L. Zeng, C. Zhang, Y. Lu, S. Qiu, C. Wang, C. Liu, L. Pan, S. Wu, J. Hu, G. Liang, P. Fan, H.-J. Egelhaaf, C. J. Brabec, F. Guo and Y. Mai, *Adv Funct Mater*, 2020, **30**, 2001240.
93. L. Zeng, Z. Chen, S. Qiu, J. Hu, C. Li, X. Liu, G. Liang, C. J. Brabec, Y. Mai and F. Guo, *Nano Energy*, 2019, **66**, 104099.
94. C. H. Li, Y. M. Pan, J. L. Hu, S. D. Qiu, C. L. Zhang, Y. Z. Yang, S. Chen, X. H. Liu, C. J. Brabec, M. K. Nazeeruddin, Y. H. Mai and F. Guo, *Acs Energy Lett*, 2020, **5**, 1386-1395.
95. C. Y. Zhang, S. Wang, H. Zhang, Y. L. Feng, W. M. Tian, Y. Yan, J. M. Bian, Y. C. Wang, S. Y. Jin, S. M. Zakeeruddin, M. Gratzel and Y. T. Shi, *Energ Environ Sci*, 2019, **12**, 3585-3594.
96. Z. L. Liu, S. B. Li, X. Wang, Y. Y. Cui, Y. Qin, S. F. Leng, Y. X. Xu, K. Yao and H. T. Huang, *Nano Energy*, 2019, **62**, 734-744.
97. J. E. Bishop, J. A. Smith, C. Greenland, V. Kumar, N. Vaenas, O. S. Game, T. J. Routledge, M. Wong-Stringer, C. Rodenburg and D. G. Lidzey, *Acs Appl Mater Inter*, 2018, **10**, 39428-39434.
98. F. Schackmar, H. Eggers, M. Frericks, B. S. Richards, U. Lemmer, G. Hernandez-Sosa and U. W. Paetzold, *Adv Mater Technol-Us*, 2020, 2000271.
99. K. Hooper, M. Carnie, C. Charbonneau and T. Watson, *Int J Photoenergy*, 2014, 953623.
100. J. Troughton, C. Charbonneau, M. J. Carnie, M. L. Davies, D. A. Worsley and T. M. Watson, *J Mater Chem A*, 2015, **3**, 9123-9127.
101. J. Troughton, M. J. Carnie, M. L. Davies, C. Charbonneau, E. H. Jewell, D. A. Worsley and T. M. Watson, *J Mater Chem A*, 2016, **4**, 3471-3476.
102. V. L. Pool, B. Dou, D. G. Van Campen, T. R. Klein-Stockert, F. S. Barnes, S. E. Shaheen, M. I. Ahmad, M. F. A. M. van Hest and M. F. Toney, *Nat Commun*, 2017, **8**, 14075.
103. Z. L. Ouyang, H. Abrams, R. Bergstone, Q. T. Li, F. Zhu and D. W. Li, *Adv Energy Mater*, 2020, **10**, 1902898.
104. P. You, G. J. Li, G. Q. Tang, J. P. Cao and F. Yan, *Energ Environ Sci*, 2020, **13**, 1187-1196.
105. S. Sanchez, X. Hua, N. Phung, U. Steiner and A. Abate, *Adv Energy Mater*, 2018, **8**, 1702915.
106. S. Sanchez, M. Valles-Pelarda, J. A. Alberola-Borras, R. Vidal, J. J. Jeronimo-Rendon, M. Saliba, P. P. Boix and I. Mora-Sero, *Mater Today*, 2019, **31**, 39-46.
107. F. Zhang and K. Zhu, *Adv Energy Mater*, 2020, **10**, 1902579.
108. S. Qiu, X. Xu, L. Zeng, Z. Wang, Y. Chen, C. Zhang, C. Li, J. Hu, T. Shi, Y. Mai and F. Guo, *J Energy Chem*, 2020, **54**, 45-52.
109. F. Guo, H. Azimi, Y. Hou, T. Przybilla, M. Y. Hu, C. Bronnbauer, S. Langner, E. Spiecker, K. Forberich and C. J. Brabec, *Nanoscale*, 2015, **7**, 1642-1649.
110. Y. X. Zhao and K. Zhu, *J Phys Chem C*, 2014, **118**, 9412-9418.
111. C. T. Zuo and L. M. Ding, *Nanoscale*, 2014, **6**, 9935-9938.
112. Y. N. Chen, Y. X. Zhao and Z. Q. Liang, *Chem Mater*, 2015, **27**, 1448-1451.
113. M. M. Tavakoli, P. Yadav, D. Prochowicz, M. Sponseller, A. Osherov, V. Bulovic and J. Kong, *Adv Energy Mater*, 2019, **9**, 1803587.
114. K. H. Stone, A. Gold-Parker, V. L. Pool, E. L. Unger, A. R. Bowring, M. D. McGehee, M. F. Toney and C. J. Tassone, *Nat Commun*, 2018, **9**, 3458.

115. Y. L. Guo, K. Shoyama, W. Sato, Y. Matsuo, K. Inoue, K. Harano, C. Liu, H. Tanaka and E. Nakamura, *J Am Chem Soc*, 2015, **137**, 15907-15914.
116. J. W. Lee, H. S. Kim and N. G. Park, *Accounts Chem Res*, 2016, **49**, 311-319.
117. N. Ahn, D. Y. Son, I. H. Jang, S. M. Kang, M. Choi and N. G. Park, *J Am Chem Soc*, 2015, **137**, 8696-8699.
118. J. L. Hu, C. Wang, S. D. Qiu, Y. C. Zhao, E. Gu, L. X. Zeng, Y. Z. Yang, C. H. Li, X. H. Liu, K. Forberich, C. J. Brabec, M. K. Nazeeruddin, Y. H. Mai and F. Guo, *Adv Energy Mater*, 2020, **10**, 2000173.
119. C. B. Fei, B. Li, R. Zhang, H. Y. Fu, J. J. Tian and G. Z. Cao, *Adv Energy Mater*, 2017, **7**, 1602017.
120. Y. Jo, K. S. Oh, M. Kim, K. H. Kim, H. Lee, C. W. Lee and D. S. Kim, *Adv Mater Interfaces*, 2016, **3**, 1500768.
121. J. W. Lee, S. H. Bae, Y. T. Hsieh, N. De Marco, M. K. Wang, P. Y. Sun and Y. Yang, *Chem-Us*, 2017, **3**, 290-302.
122. L. F. Zhu, Y. Z. Xu, P. P. Zhang, J. J. Shi, Y. H. Zhao, H. Y. Zhang, J. H. Wu, Y. H. Luo, D. M. Li and Q. B. Meng, *J Mater Chem A*, 2017, **5**, 20874-20881.
123. Y. Z. Wu, F. X. Xie, H. Chen, X. D. Yang, H. M. Su, M. L. Cai, Z. M. Zhou, T. Noda and L. Y. Han, *Adv Mater*, 2017, **29**, 1701073.
124. T. Q. Niu, J. Lu, R. Munir, J. B. Li, D. Barrit, X. Zhang, H. L. Hu, Z. Yang, A. Amassian, K. Zhao and S. Z. Liu, *Adv Mater*, 2018, **30**, 1706576.
125. T. H. Wu, Y. B. Wang, X. Li, Y. Z. Wu, X. Y. Meng, D. Y. Cui, X. D. Yang and L. Y. Han, *Adv Energy Mater*, 2019, **9**, 1803766.
126. Z. G. Xiao, Q. F. Dong, C. Bi, Y. C. Shao, Y. B. Yuan and J. S. Huang, *Adv Mater*, 2014, **26**, 6503-6509.
127. C. Liu, K. Wang, C. Yi, X. J. Shi, A. W. Smith, X. Gong and A. J. Heeger, *Adv Funct Mater*, 2016, **26**, 101-110.
128. L. Gouda, R. Gottesman, S. Tirosh, E. Haltzi, J. G. Hu, A. Ginsburg, D. A. Keller, Y. Bouhadana and A. Zaban, *Nanoscale*, 2016, **8**, 6386-6392.
129. H. Yu, X. D. Liu, Y. J. Xia, Q. Q. Dong, K. C. Zhang, Z. W. Wang, Y. Zhou, B. Song and Y. F. Li, *J Mater Chem A*, 2016, **4**, 321-326.
130. M. J. Yang, T. Y. Zhang, P. Schulz, Z. Li, G. Li, D. H. Kim, N. J. Guo, J. J. Berry, K. Zhu and Y. X. Zhao, *Nat Commun*, 2016, **7**, 12305.
131. D. Y. Luo, W. Q. Yang, Z. P. Wang, A. Sadhanala, Q. Hu, R. Su, R. Shivanna, G. F. Trindade, J. F. Watts, Z. J. Xu, T. H. Liu, K. Chen, F. J. Ye, P. Wu, L. C. Zhao, J. Wu, Y. G. Tu, Y. F. Zhang, X. Y. Yang, W. Zhang, R. H. Friend, Q. H. Gong, H. J. Snaith and R. Zhu, *Science*, 2018, **360**, 1442-1446.
132. J. Lee, H. Kang, G. Kim, H. Back, J. Kim, S. Hong, B. Park, E. Lee and K. Lee, *Adv Mater*, 2017, **29**, 1606363.
133. S. S. Zhang, M. Stolterfoht, A. Armin, Q. Q. Lin, F. S. Zu, J. Sobus, H. Jin, N. Koch, P. Meredith, P. L. Burn and D. Neher, *Acs Appl Mater Inter*, 2018, **10**, 21681-21687.
134. X. W. Xu, C. Q. Ma, Y. H. Cheng, Y. M. Xie, X. P. Yi, B. Gautam, S. M. Chen, H. W. Li, C. S. Lee, F. So and S. W. Tsang, *J Power Sources*, 2017, **360**, 157-165.
135. H. S. Lee, M. K. Kim, S. R. Pae, D. Kim, H. Seo, P. Boonmongkolras, I. Gereige, S. Park and B. Shin, *Nano Energy*, 2020, **74**, 104830.
136. M. A. Green, E. D. Dunlop, D. H. Levi, J. Hohl-Ebinger, M. Yoshita and A. W. Y. Ho-Baillie, *Prog Photovoltaics*, 2020, **28**, 3-15.
137. Z. P. Wang, D. P. McMeekin, N. Sakai, S. van Reenen, K. Wojciechowski, J. B. Patel, M. B. Johnston and H. J. Snaith, *Adv Mater*, 2017, **29**, 1604186.

138. Q. Yao, Q. F. Xue, Z. C. Li, K. C. Zhang, T. Zhang, N. Li, S. H. Yang, C. J. Brabec, H. L. Yip and Y. Cao, *Adv Mater*, 2020, **32**, 2000571.
139. P. Gao, A. B. Yusoff and M. K. Nazeeruddin, *Nat Commun*, 2018, **9**, 5028.
140. D. H. Cao, C. C. Stoumpos, O. K. Farha, J. T. Hupp and M. G. Kanatzidis, *J Am Chem Soc*, 2015, **137**, 7843-7850.
141. S. Chen, N. Shen, L. Z. Zhang, W. G. Kong, L. H. Zhang, C. Cheng and B. M. Xu, *J Mater Chem A*, 2019, **7**, 9542-9549.
142. S. Chen, N. Shen, L. H. Zhang, L. Z. Zhang, S. H. Cheung, S. M. Chen, S. K. So and B. M. Xu, *Adv Funct Mater*, 2020, **30**, 1907759.
143. T. Q. Niu, J. Lu, M. C. Tang, D. Barrit, D. M. Smilgies, Z. Yang, J. B. Li, Y. Y. Fan, T. Luo, I. McCulloch, A. Amassian, S. Z. Liu and K. Zhao, *Energ Environ Sci*, 2018, **11**, 3358-3366.
144. P. Chen, Y. Bai, S. C. Wang, M. Q. Lyu, J. H. Yun and L. Z. Wang, *Adv Funct Mater*, 2018, **28**, 1706923.
145. J. Z. Chen, J. Y. Seo and N. G. Park, *Adv Energy Mater*, 2018, **8**, 1702714.
146. F. Bella, G. Griffini, J. P. Correa-Baena, G. Saracco, M. Gratzel, A. Hagfeldt, S. Turri and C. Gerbaldi, *Science*, 2016, **354**, 203-206.
147. X. J. Huang, Q. Y. Guo, D. D. Yang, X. D. Xiao, X. F. Liu, Z. G. Xia, F. J. Fan, J. R. Qiu and G. P. Dong, *Nat Photonics*, 2020, **14**, 82-88.
148. J. L. Duan, Y. Y. Zhao, X. Y. Yang, Y. D. Wang, B. L. He and Q. W. Tang, *Adv Energy Mater*, 2018, **8**, 1802346.
149. W. Li, M. U. Rothmann, A. Liu, Z. Y. Wang, Y. P. Zhang, A. R. Pascoe, J. F. Lu, L. C. Jiang, Y. Chen, F. Z. Huang, Y. Peng, Q. L. Bao, J. Etheridge, U. Bach and Y. B. Cheng, *Adv Energy Mater*, 2017, **7**, 1700946.
150. R. J. Sutton, G. E. Eperon, L. Miranda, E. S. Parrott, B. A. Kamino, J. B. Patel, M. T. Horantner, M. B. Johnston, A. A. Haghighirad, D. T. Moore and H. J. Snaith, *Adv Energy Mater*, 2016, **6**, 1502458.
151. C. Liu, W. Z. Li, J. H. Chen, J. D. Fan, Y. H. Mai and R. E. I. Schropp, *Nano Energy*, 2017, **41**, 75-83.
152. Y. Y. Fan, J. J. Fang, X. M. Chang, M. C. Tang, D. Barrit, Z. Xu, Z. W. Jiang, J. L. Wen, H. Zhao, T. Q. Niu, D. M. Smilgies, S. Y. Jin, Z. K. Liu, E. Q. Li, A. Amassian, S. Z. Liu and K. Zhao, *Joule*, 2019, **3**, 2485-2502.